Science Advances
AAAS

advances.sciencemag.org/cgi/content/full/6/38/eaba8940/DC1

Supplementary Materials for

Human footprints provide snapshot of last interglacial ecology in the Arabian interior

Mathew Stewart*, Richard Clark-Wilson*, Paul S. Breeze, Klint Janulis, Ian Candy, Simon J. Armitage, David B. Ryves,
Julien Louys, Mathieu Duval, Gilbert J. Price, Patrick Cuthbertson, Marco A. Bernal, Nick A. Drake,
Abdullah M. Alsharekh, Badr Zahrani, Abdulaziz Al-Omari, Patrick Roberts, Huw S. Groucutt, Michael D. Petraglia*

*Corresponding author. Email: mstewart@ice.mpg.de (M.S.);
richard.clark-wilson@rhul.ac.uk (R.C.-W.); petraglia@shh.mpg.de (M.D.P.)

Published 18 September 2020, *Sci. Adv.* **6**, eaba8940 (2020)
DOI: 10.1126/sciadv.aba8940

This PDF file includes:

- Supplementary Texts S1 to S6
- Figs. S1 to S13
- Tables S1 to S17
- References

Supplementary Text 1: Sedimentology and diatom analysis

Site context. The Alathar paleolake deposit (site code: WNEF17_1) is situated within an interdunal depression in the southwestern Nefud Desert, approximately 85 km southeast from the city of Tayma, Saudi Arabia (27˚ 31' 11.8''; E 39˚ 23' 55.0''; altitude 955 msl). The deposit sits as an inverted relief feature, rising above the modern basin floor, and comprises a ~1.8 m thick palaeolake deposit overlying aeolian dune sands (Fig. S1). The topography of the paleolake is well preserved with a subtle concave shape dipping toward the centre of the remaining palaeolake deposit.

Macroscale sedimentology. The site was initially surveyed in order to identify the best exposed stratigraphic sequence for further analysis. Two sedimentary sections were recorded at the site and a composite section formed (Fig. 3). The two sections are located ~30 meters apart, and the relationship between them is clearly visible in the field. Each section was logged and described to determine the sedimentary structure (bedding and units) and texture (sorting, grain size, and colour). The first section (Section 1; ~142 cm in height; Units 2–4) is located on the western margin of the relict paleolake deposit and faces the lee side of the dune to the east. Here the palaeolake sequence is at its thickest, suggesting that the lake depocenter lay toward the west but has since been eroded. A second section (Section 2; ~39 cm in height; Units 5–7) that stratigraphically lies above the first section was logged near the centre of the modern-day surface of the palaeolake deposit.

Unit 1 is composed of loose sands that underlie the first paleolake section. The first paleolake section is ~142 cm in height and consists of three discrete units (Units 2–4). Unit 2 (0 – 65 cm) is ~65 cm thick and consists of loosely consolidated sandy-silt diatomite with some evidence for horizontal bedding. There is also evidence of orange coloured, thin, elongate mottling. Unit 3 (65 – 103 cm) is ~38 cm thick and is characterised by horizontally-bedded sandy-silt diatomite that interdigitates with sand layers. Obvious orange mottling continues, as does centimetre-scale root casts that run between the horizontal diatomite bedding planes. The unit ends with a ~3 cm laterally discontinuous desiccation crack (103 – 106 cm). Unit 4 (106 – 142 cm) is split into two sub-units. Unit 4a (~106–125 cm) is formed of consolidated and horizontally bedded sandy-silt diatomite that interdigitates with laterally continuous sand layers. There is no evidence of mottling or root casts, while the sediment is almost pure white. Unit 4b (~125–142 cm) is a structureless, pure white sandy-silt diatomite that is consolidated, has no horizontal bedding features, and contains desiccation cracks. It is in the upper surface of this unit that footprints and *in situ* fossils were found.

The second section (~142–181 cm; Units 5–7), which lies ~30 m from the first section and stratigraphically overlies it and therefore the prints, is divided into three units. Unit 5 (142 – 163 cm) is ~21 cm thick and consists of a sandy-silt diatomite that interdigitates with bedded sands. Unit 6 (163 – 177 cm) is ~14 cm thick and composed of sands with laterally discontinuous but consolidated sandy-silt diatomite beds with reworked rip-up diatomite clasts. Unit 7 (177 – 181 cm) is 4 cm thick and is composed of homogenous sandy-silt diatomite.

Micromorphology. Fourteen thin-sections were taken across both sections and show little compositional variability (Fig. S2 & S3). All contained sub-angular to well-rounded sand grains that ranged from medium silts to very coarse sands (based on measuring the smallest and largest sand grains in each slide in thin-section), frequent diatoms/sponge spicules and a fine-grained, brown siliceous amorphous matrix. The main variation across the sedimentary sequences is in the grain to matrix ratio. The lower two thin-sections from Unit 1, which comprise loosely consolidated sandy-silt diatomite, have no evidence of structure and contain the most densely packed allogenic silt and sand grains (~50% cover). The thin-sections in the following units are densely packed with allogenic grains (~25–33% cover) but contain bands or patches where the density of quartz grains is much less (~5–10% cover), while there is a notable decrease in allogenic grains in Unit 4b and all units in section 2 (Units 5 – 7) (see Fig S3). There is no evidence of iron-staining except for the lowermost thin-section from Unit 2 and Unit 4. Organic material is rare, with occasional amorphous organic materials in some thin-sections (though showing no trend throughout the sequence) and a single section with rare evidence of organics with cellular preservation.

Diatoms. Results of the diatom analysis are presented in Figure S4. There is good coverage between fossil and modern training sets. Goodness-of-fit was assessed by considering the proportion of fossil data used in each sample for reconstructions, and the minimum dissimilarity coefficient (MinDC) between each fossil sample and the training set. Other studies have suggested that good analogues exist in a training set where MinDC is 100–150 or less (*33, 67*). Within the EDDI African database, species coverage between the fossil and modern datasets is between 93-96%, and MinDC for all samples was below the 2% percentile for DCs within the training set (MinDC between 87 (175 cm) – 107 (40 cm)). We therefore consider the diatom-inferred conductivity to be reliable estimates of (sample mean) paleoconductivity at the WNEF_17 site.

Diatom samples are well preserved with **F** index values (the ratio of pristine to all valves; *68, 69*) between 0.73–0.77 in all three levels. The assemblages all suggest relatively oligotrophic (low nutrient availability) and freshwater conditions, although there are subtle differences between them and hence inferred aquatic environments. All assemblages are dominated by *Fragilaria sensu lato* (*Pseudostaurosira brevistriata*, *Staurosira constuens* agg. and *S. pinnata*), accounting for between 74–87% of the assemblage, a proportion which increases systematically from the basal unit (40 cm) to the uppermost sample (175 cm). Additionally, the basal sample has significant (but low) abundances of more brackish taxa such as *Amphora copulata* and *Navicula oblonga*, although taxa typical of freshwater habitats are also found, including *Cymbella* and (tychoplanktonic) *Ulnaria* spp. (the latter seen in all three samples). Some valves of freshwater plankton were also encountered, such as *Cyclotella* (now *Lindavia*) *ocellata* and the more mesotrophic *Aulacoseira granulata* and *A. ambigua* (with both *Aulacoseira* species present in all three samples). *Lindavia ocellata* is typical of oligotrophic lakes in Europe today across a range of lake depths but is also found in Ethiopian lakes at the start of the Holocene at the onset of the African Humid Period (*70*), whereas *A. granulata* typically occurs in deeper and well-mixed lakes, but can also be found in more shallow and turbid systems (including rivers). This suggests the assemblage covers a range of lake conditions, although water levels remained fairly shallow and fresh throughout.

The middle sample (140 cm) has a similar assemblage composition, with lower abundance of more saline taxa (e.g. *A. copulata* declines and *N. oblonga* disappears), while some valves of the aerophilous *Hantzschia amphioxys* were observed. Valve breakage is slightly greater in this sample and valve dissolution, as indicated by sample **F** scores, declines slightly, suggesting this period may perhaps have experienced greater water level fluctuation (and greater sediment in-wash and turbulent mixing) than other samples. The uppermost sample has many of the same benthic taxa as the other samples but additionally includes the brackish planktonic taxon *Thalassiosira pseudonana*, while *L. ocellata* was not observed.

Diatom-inferred conductivity for all samples suggest freshwater conditions in all cases with values ranging between 220 μS cm^{-1} (140 cm) and 350 μS cm^{-1} (175 cm). All samples also contain chrysophyte cysts, supporting an interpretation of freshwater and generally low/medium nutrient conditions in all sections, though the chrysophyte:diatom ratio and effective species diversity (Hill's N_2) both fall consistently throughout the sequence from 40 cm to 175 cm. It is perhaps noteworthy that minimum conductivity is inferred for the middle sample, coinciding with the level at which the hominid footprints were found. Given the very good diatom preservation, it is also likely that the lake rarely completely dried out in any of the periods represented by the three samples, as diatom preservation is known to be much worse in such ephemeral systems (e.g. *71–72*).

Depositional model. The interpretation provided by the diatom paleoecology is supported by the sedimentary analysis. Semi-quantitative XRD shows the mineralogy is composed of 91–100 % quartz and K-feldspar (0–9 %), while no evaporitic minerals (i.e., gypsum or halite) are present. This suggests that the water body was unlikely to be brackish or saline. Likewise, the sediments suggest changes in lake extent and depth with evidence of episodic drying events. This is shown by horizontal bedding with laterally continuous sandy-silt diatomite interdigitated with laterally continuous sand layers. These characteristics are present in Units 2, 3, 4a, and 5. The sandy-silt diatomite is indicative of sedimentation during a wetter phase within a shallow freshwater lake. Sand beds were then deposited during more arid phases when lake levels dropped.

The presence of vegetation is evidenced by thin-elongate mottling in Units 2, 3, and 5, which typically results from local chemical and biological heterogeneities where organic matter has been oxidised (*73*). Further evidence for vegetation is shown by the presence of root casts that run between the horizontally bedded diatomite layers in Unit 3. Vegetation growth may have been post-depositional or occurred during the deposition of these units. In the latter case, this would suggest a slow sedimentation rate and shallow waters, which is consistent with the diatom paleoecology from Alathar. Mottling and root casts are not present in Units 4a, 4b, 6, or 7, indicating a reduction in vegetation at the site during the deposition of these units. This may reflect more turbulent and shallow conditions, which inhibit aquatic plant growth (*74*), and is consistent with the Unit 4b diatom assemblage.

Unstable conditions in the local environment are indicated by the constant influx of medium-silt to very-coarse allogenic sand grains throughout the sequence. All sections contain significant quantities of moderately to well-sorted allogenic sand and silt grains within a brown, amorphous matrix, though the relative proportion of allogenic grains to matrix reduces moving upwards through the sequence. This is also reflected in the cohesion of the sediment through the sequence, where sediment from Unit 2 was friable whereas all other units above it were more consolidated. This most likely suggests that at the onset of the pluvial phase the landscape immediately surrounding the lake was unstable with limited vegetation cover to stabilise surficial dune sands, but gradually stabilised reducing the amount of available material to be transported into the lake basin. Nevertheless, the total amount of allogenic sand/silt grains through the sequence at Alathar is in contrast to the nearby Al Wusta site, where allogenic sand- to silt-sized grains are rare (*4*). It is not clear whether the locally unstable environment at Alathar is a consequence of local hydrological factors (Alathar is more elevated and situated further from the edge of the present-day dune field) or reflects different climatic conditions during its existence.

In summary, the Alathar sediments are interpreted as recording the presence of a perennial oligotrophic/mesotrophic shallow freshwater lake that was subject to occasional desiccation. Perhaps the two most important observations are that: (1) the footprints lie within the lacustrine deposit and, therefore, demonstrate the presence of hominins in Arabia within a humid phase; and (2) the water body was fresh and, therefore, provided a vital resource for hominins and fauna in the western Nefud Desert, Saudi Arabia. Further research at the site, or of nearby similar paleolake deposits, may elucidate the role, or lack thereof, that seasonal fluctuations in humidity and precipitation played in regulating the Arabian lakes during the Pleistocene.

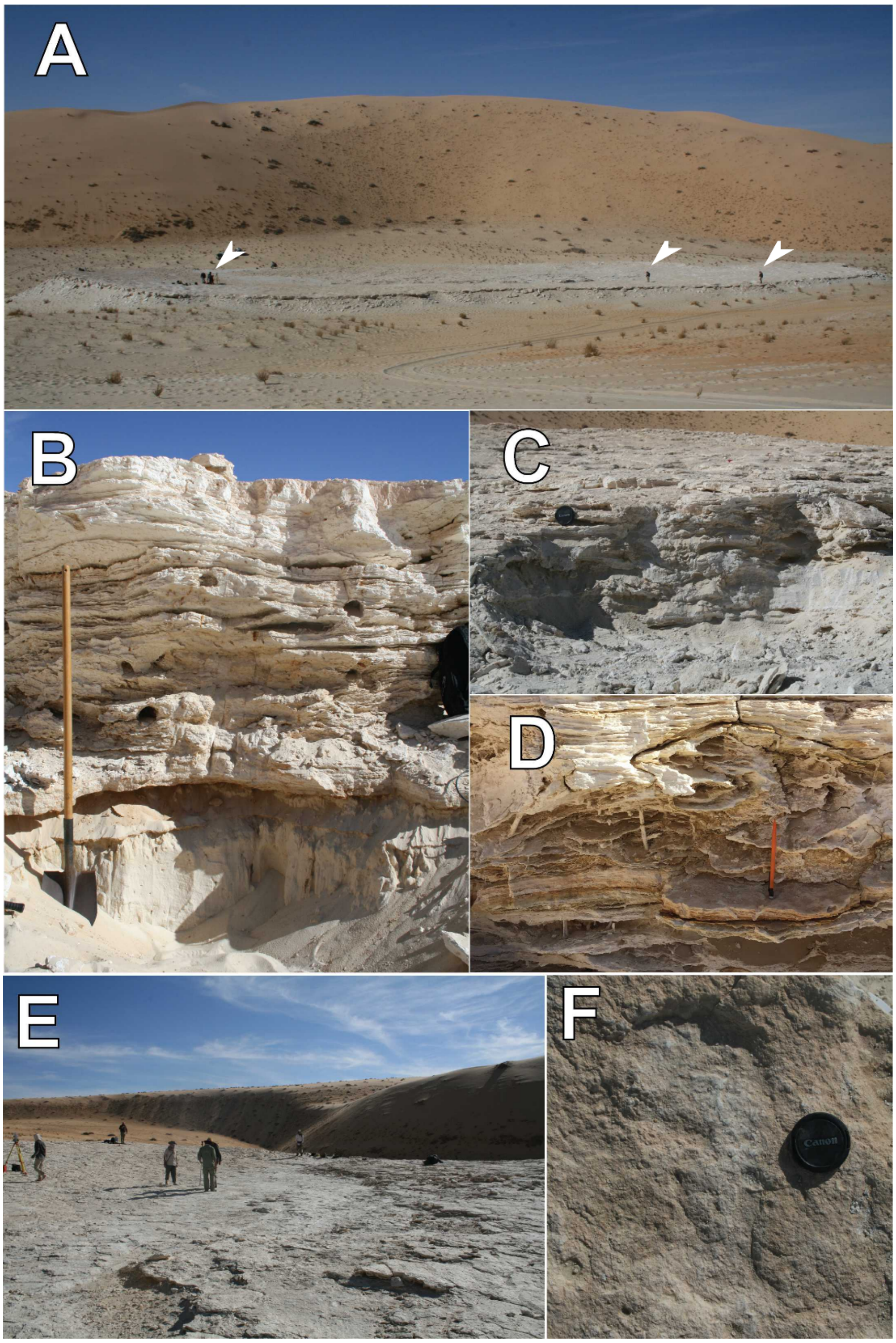

Figure S1. (A) Plan view of the Alathar paleolake deposit, researchers indicated by arrows. **(B)** First stratigraphic section (Units 2–4). **(C)** Second section (Units 5–7) overlying the first but located towards the centre of the paleolake. **(D)** Root cases running between horizontal diatomite bedding planes in Unit 3. **(E)** Looking southwards across the palaeolake surface. Small ridge in the centre of this picture contains the logged second section (~39 cm) which stratigraphically overlies the footprints. **(F)** Hominin print within the top of the first section (Unit 4b). Photo credit: Richard Clark-Wilson, Royal Holloway, University of London.

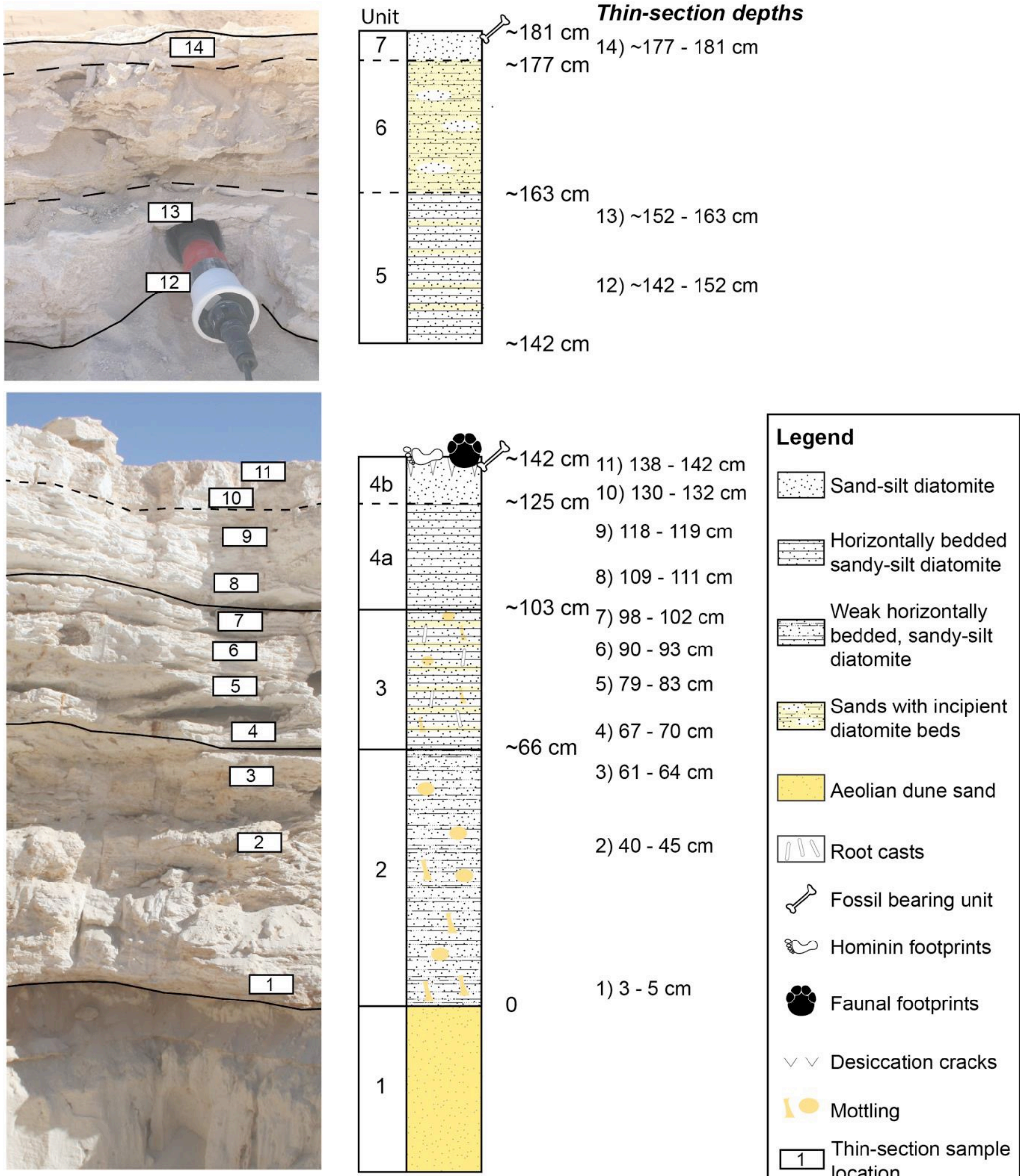

*note that images are not at the same scale.

Figure S2. Sedimentary sequence at Alathar with the location of the thin-section samples highlighted. Photo credit: Richard Clark-Wilson, Royal Holloway, University of London.

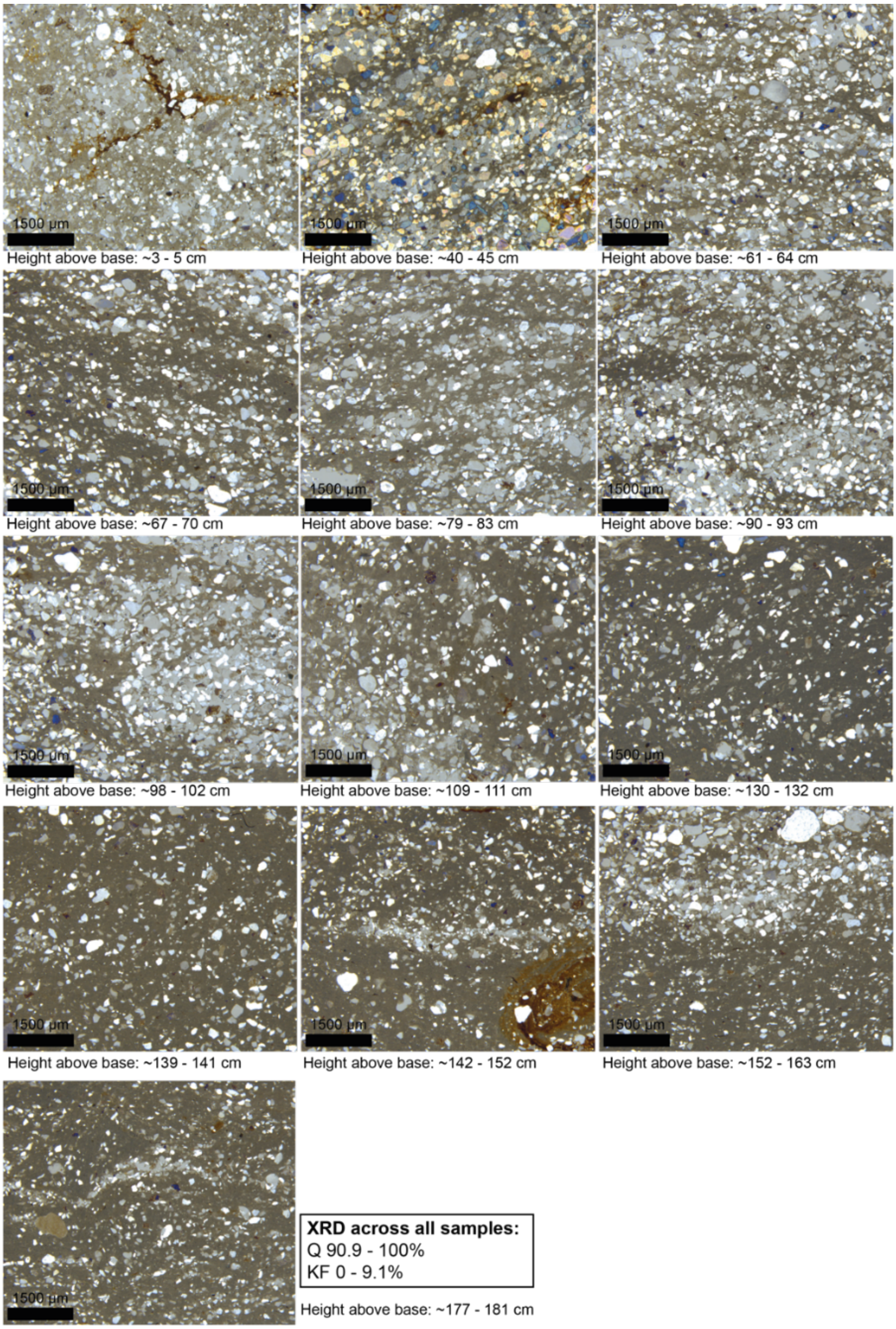

Height above base: ~3 - 5 cm
Height above base: ~40 - 45 cm
Height above base: ~61 - 64 cm
Height above base: ~67 - 70 cm
Height above base: ~79 - 83 cm
Height above base: ~90 - 93 cm
Height above base: ~98 - 102 cm
Height above base: ~109 - 111 cm
Height above base: ~130 - 132 cm
Height above base: ~139 - 141 cm
Height above base: ~142 - 152 cm
Height above base: ~152 - 163 cm
Height above base: ~177 - 181 cm

Figure S3. Photo-micrographs in cross-polarised light of Alathar palaeolake sediments. Note that the sediment closest to the base of the sequence is pictured in the top-left panel, and as the panels move from left – right along rows and then down columns the sedimentary sequence moves upwards. Photo credit: Richard Clark-Wilson, Royal Holloway, University of London.

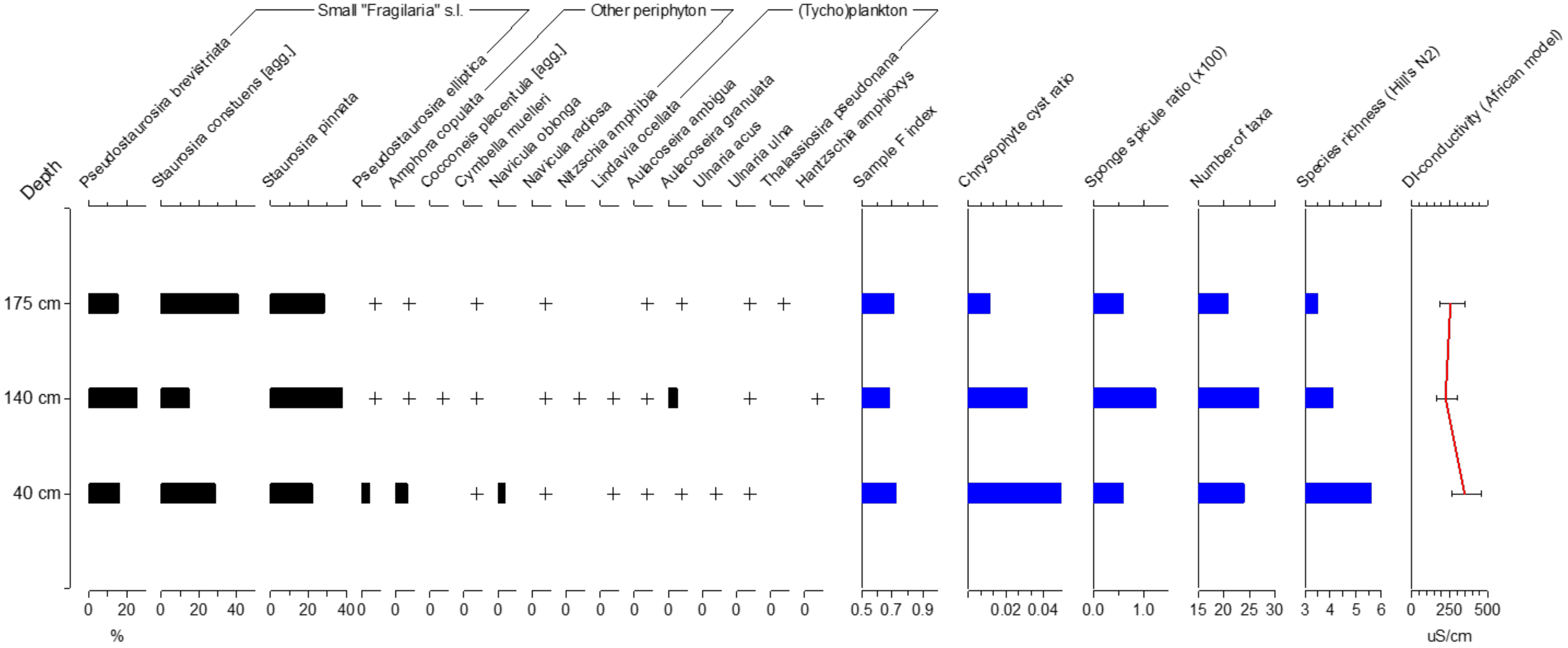

Figure S4. Diatoms analysis for site WNEF17_1. All taxa present at >3% are included, as well as ecologically significant taxa (black bars). All occurrences <3% indicated with a "+". Blue bars represent other metrics derived from counting including chrysophyte cyst:diatom and sponge spicule:diatom ratios, and assemblage diatom species richness (as total number of taxa and effective richness as Hill's N_2). Diatom inferred conductivity is also shown for the three sample, with sample-specific errors. See text for more details

Supplementary Text 2: Optically stimulated luminescence (OSL) dating

Sample collection and preparation. Three samples were collected for luminescence dating. One sample (PD60) was taken from the aeolian dune sands underlying the palaeolake deposits (Unit 1), another sample (PD61) from Unit 2 within the main palaeolake sequence, and a final sample (PD62) from Unit 5, which stratigraphically overlies the footprints and *in situ* fossils. PD60 was taken by hammering an opaque tube into a cleaned section face, whereas PD61 and PD62 were extracted as consolidated blocks. Samples were prepared under subdued red light in the Royal Holloway Luminescence Laboratory. First the sunlight exposed external portions of the sample were removed and retained for dose rate evaluation, leaving a sub-sample suitable for dating. The sample for dating was immersed in 10% HCl to remove any carbonate, but since no organic matter was present, samples were not treated with H_2O_2. The remaining mineral fraction was disaggregated in dilute sodium hexametaphosphate solution and wet-sieved to 180–210 µm. Quartz was extracted from the retained fraction using density separations at 2.75 and 2.62 g/cm3 and a subsequent HF acid etch (23M HF for 60 min followed by a 24-hour immersion in 10M HCl). Etched samples were re-sieved at 150 µm, to remove partially dissolved grains, and stored in opaque containers prior to measurement. Purified quartz was mounted as a monolayer on 9.7 mm diameter stainless steel discs using Silkospray oil applied via a 5 mm mask.

Equipment. All luminescence measurements presented here were carried out using a Risø TL/OSL-DA-15 automated dating system (*37*). Optical stimulation of aliquots was carried out using blue (470 nm) light emitting diodes with a stimulation power of 69.4 mW/cm^2. All infra-red (IR) stimulation was carried out using an IR (870 nm) laser diode array yielding a power density of 206mW/cm^2. OSL passed through 7.5 mm of Hoya U-340 filter and was detected using an Electron Tubes Ltd 9235QB15 photomultiplier tube. Irradiation was carried out using a 40 mCi ^{90}Sr/^{90}Y beta source giving ~6 Gy/min. This source is calibrated relative to the National Physical Laboratory, Teddington ^{60}Co γ-source (Hotspot 800, *75*).

Single-aliquot measurement and analysis. Equivalent doses (D_e) were estimated by measuring 48 aliquots of each sample using the single-aliquot regenerative-dose (SAR) method (*38*). To ensure that the measurement conditions were optimal, dose recovery tests (*76*) were performed on samples PD61 and PD62 using a known dose of ~108 Gy. A preheating regime of 200°C held for 10 seconds prior to the measurement of the natural (L_n)/regenerated (L_x) signal, and 160°C held for 5 seconds prior to measurement of the test dose (T_x) signal gave dose recovery ratios of 1.02 ± 0.02 for PD61 and 1.01 ± 0.04 for PD62. Subsequent D_e measurements were performed using this preheating regime. Optical stimulation was carried out at 125°C for 60 seconds using blue LEDs. The OSL signal was calculated from the signal from the first 0.32 seconds of stimulation, with a background signal estimated from the last 4 seconds of the decay curve subtracted. Dose response curves (DRC) were fitted with a saturating-exponential-plus-linear function, and the standard error associated with each individual D_e determination was estimated by Monte Carlo simulation (1000 simulations). D_e determination, curve fitting and Monte Carlo simulation were performed using Luminescence Analyst software version 4.31.9 (*77*).

In common with previously reported studies of quartz from the Nefud Desert (e.g. Petraglia et al., 2012; Groucutt et al., 2018), the Alathar samples have a relatively low intrinsic sensitivity but the initial OSL decays rapidly, consistent with a fast component dominated signal. Each aliquot contained ~416-429 grains at the 95% confidence interval, calculated using the calc_AliquotSize function in the R luminescence package assuming 0.65 packing density (*78*). Although single-grain measurements have not been carried out in the present study, single-grain data from the nearby site of Al Wusta (*4*) are likely to be representative of the situation at Alathar, since at both sites the quartz is derived from the Nefud dune field. At Al Wusta, only ~6% of grains yield a measurable luminescence signal (the OSL signal from the grain is distinguishable from the variability in the background signal, determined using the “Tn signal more than 3 sigma above BG” rejection criterion in Luminescence Analyst), while only ~1.5% of grains yielded acceptable luminescence characteristics (*4*). Assuming these proportions hold true for Alathar, individual aliquots should contain on average ~25 grains emitting a measurable luminescence signal of which only ~6 have acceptable luminescence characteristics.

Data from individual aliquots were rejected where the aliquot yielded either an IR depletion ratio >2σ below unity (*79*) or a recycling ratio >2σ different from unity (*37*). These standard tests reject aliquots with significant feldspar contamination, or which have poor luminescence properties respectively, and are routinely applied in the majority of luminescence studies. In addition, aliquots yielding natural luminescence intensities very near to or greater than the saturation level of the growth curve (i.e. “oversaturated” aliquots) were rejected. Although a considerable body of literature concerning saturated/oversaturated aliquots exists, and various rejection criteria have been proposed, there is little consensus on the most appropriate method for dealing with this phenomenon. Consequently, while numerous studies recognise the need to reject saturated/oversaturated aliquots or grains, no standard criterion exists. To determine the sensitivity of the Alathar ages to different saturation/oversaturation rejection criteria, three separate analyses were performed(Table S1): (1) accept all aliquots for which Analyst generates a finite D_e; (2) reject all aliquots yielding natural luminescence intensities (L_n/T_n) exceeding twice the curve fitting parameter D_o when the DRC is fitted using a single saturating exponential function (*80*); (3) reject aliquots where the natural luminescence intensity (L_n/T_n) exceeds the saturation level of a saturating exponential fit (using Analyst version 4.31.9) or, when fitted with a saturating-exponential-plus-linear function, where L_n/T_n exceeds 115% of L_x/T_x for the highest-dose regeneration point. The second criterion within Approach 3 is an attempt to codify the well-established practice of excluding data from aliquots which are clearly saturated/oversaturated, but for which the linear component of a saturating-exponential-plus-linear curve fit yields a finite D_e. It is only applicable where the largest regeneration dose is substantially higher than the sample's burial dose. In the present instance, the largest regeneration dose was 195 Gy and the largest sample burial dose (calculated using Approach 1) was 127±10 Gy. Approach 1 includes very high D_e values and probably overestimated D_e due to the incorporation of saturated aliquots. This approach may be regarded as generating a maximum age. Approach 2 excludes aliquots yielding high D_es, some of which may provide accurate estimates of the absorbed dose. This approach may be regarded as generating a minimum age (see Ref *81* p. 24 for discussion). Approach 3 is less stringent than Approach 2, and in the present study always yields D_e values lying between the other two options. We prefer the sample burial dose produced using Approach 3, since Approach 1 probably yields overestimates while Approach 2 may yield underestimates. We note that for PD61 and PD62, the samples which constrain the age of the mammalian tracks at Alathar, all three approaches yield ages consistent with the first half of MIS5. Furthermore, only Approach 2 yields an age which is not consistent (at 1σ) with MIS5e, and then only for the sample (PD62) which overlies and therefore postdates the mammalian tracks. Our analysis shows that the ages of the Alathar samples are not particularly sensitive to the precise saturation/oversaturation rejection criterion used.

Details of accepted and rejected aliquots are presented in Table S2. Briefly, rejection criteria were applied in order, with only one rejection criterion being recorded per aliquot. Of the 144 aliquots measured, 2 failed the recycling ratio test, 69 failed the IR-depletion ratio test and 10 were oversaturated, leaving 63 accepted aliquots. Several previous studies of quartz from the Nefud Desert have reported similarly high IR-depletion ratio test failure rates (e.g. *4*, *16*). In Ref *4*, samples were subjected to a one-week H_2SiF_6 treatment followed by HCl rinse in addition to the HF etch, in an attempt to minimize feldspar contamination (see their S.I. Section 3.1), but their IR-depletion ratio failure rate for single-grains remained high. Consequently, out hypothesis is that feldspar inclusions within quartz grains are responsible for the high IR-depletion ratio test failure rates observed for Nefud sands. However, we cannot exclude the possibility that other IR sensitive, HF/H_2SiF_6 resistant, minerals are responsible (*79*).

To determine the age of a sample, a single-burial dose (D_b) must be calculated from the accepted single-aliquots. Because the samples are either well-bleached aeolian dune sands, or sands derived from such sands, D_b was calculated for all samples using the central age model (CAM) in the R luminescence package (*82–83*). Using this package, calculated overdispersion (OD) values ranged from 28±5 to 39±5. The OD values are relatively high for single-aliquot samples from aeolian dune sands (PD60) and sands within the lake sediments that derive from the surrounding dunes (PD61 and PD62). The main cause of overdispersion in these samples is unclear. Partial bleaching is unlikely to have occurred in the case of the aeolian sand sample (PD60), and the sand in samples PD61 and PD62 are likely to have been introduced to their depositional environment via aeolain/fluvial mobilisation of well-bleached surficial sands. Post-depositional mixing (“bioturbation”) of samples PD61 and PD62 is unlikely given that both were consolidated via desiccation shortly after deposition, precluding the introduction of much younger/older grains. Beta microdosimetry alone has recently been shown to be capable of causing single-grain overdispersion exceeding 25% (*83*), and is probably the primary cause of the high values measured in the present study. This inference is supported by the low environmental dose rates for Alathar palaeolake samples (0.4–1.1 Gy/ka) while there is a low concentration of K-feldspar identified by XRD analysis. Modelling by Ref *84* has demonstrated that these factors (i.e. low total does rate combined with the presence of K-feldspars) may yield high overdispersion values even for well-bleached, unmixed sediments, since the sparse K-feldspars act as local “hotspots” of beta dose. We regard this scenario as the most plausible explanation of the high overdispersion observed in our datasets, in which case the CAM is the most appropriate age model to use for the Alathar palaeolake samples (*85*). See Table S4 for summary dating results and ages.

Environmental dose rate calculations. The environmental dose rate for HF etched quartz grains consists of external beta, gamma and cosmic ray components (Table S3). Beta dose rates were measured using a Risø GM-25-5 low-level beta counting system (*39*), using MgO and Volkagem loess (*40*) standards. Gamma dose rates were measured in the field using an EG&G Ortec digi Dart-LF gamma-spectrometer using the "threshold" method. Dose rates were corrected for beta attenuation (*86*), the etch depth (*87*), grain size and a water content of 5±2.5%. The 2σ uncertainty on water content encompasses completely dry conditions (0% moisture) and saturation for 25% of the burial period (10% moisture, assuming a saturation water content of ~37%, *88*), representing the full range of reasonable mean water content scenarios for our samples. Cosmic ray dose rates were calculated using site location (27N, 39°E, ~955 m elevation) and present-day sediment burial depths (*41*), assuming a sediment overburden density of 1.80 g/cm^3. Note that the sediment burial depths used to calculate the cosmic ray dose rate are reported relative to the local ground surface, and therefore some values differ from apparent depths in the composite stratigraphy (Fig. 3). The total environmental dose rate and final age estimates were calculated using Dose Rate and Age Calculator (*89*).

Age interpretation. The dating results presented here suggest that the Alathar paleolake existed at some point between 121 ± 11 ka (PD61; Unit 2) and 112 ± 10ka (PD62; Unit 5). Following the orbital monsoon hypothesis, where increased summer insolation at 30°N extends the northerly range of monsoonal rainfall, it is most likely that the Alathar lake formed in association with the northern hemisphere summer insolation maximum at c. 128 ka during MIS 5e. The underlying sands (Unit 1) date to 255 ± 27 ka and likely relate to a phase of dune activity and aridity during MIS 8.

Table S1. Age variations for each sample depending on oversaturation rejection criteria (see SI Text 2 for full discussion). Oversaturation rejection criteria: (1) accept all aliquots for which Analyst generates a finite D_e; (2) reject all aliquots yielding natural luminescence intensities (L_n/T_n) exceeding twice the curve fitting parameter D_o when the DRC is fitted using a single saturating exponential function (*80*); (3) reject aliquots where the natural luminescence intensity (L_n/T_n) exceeds the saturation level of a saturating exponential fit (using Analyst version 4.31.9) or, when fitted with a saturating-exponential-plus-linear function, where L_n/T_n exceeds 115% of L_x/T_x for the highest-dose regeneration point.

Sample	**Saturation/oversaturation rejection criteria**	**D_b calculation method (n)**	**CAM D_b (Gy)**	**OD (%)**	**Total dose rate, D_r (Gy/ka)**	**Age (ka)**
PD60	1	CAM (17)	125±14	41±8	0.44±0.02	286±34
	2	CAM (12)	96±7	20±5	0.44±0.02	221±19
	3	CAM (15)	111±10	34±7	0.44±0.02	255±27
PD61	1	CAM (19)	124±10	32±6	0.95±0.04	130±12
	2	CAM (14)	109±9	26±5	0.95±0.04	115±10
	3	CAM (16)	115±9	28±5	0.95±0.04	121±11
PD62	1	CAM (36)	127±10	41±5	1.08±0.05	118±11
	2	CAM (21)	104±9	38±6	1.08±0.05	97±10
	3	CAM (32)	121±9	39±5	1.08±0.05	112±10

Table S2. The number of single aliquots which were measured, rejected after application of the criteria outlined in Table S1 and accepted for inclusion in the calculation of D_b. Samples indicated (DR) represent dose recovery data.

Sample	**PD61 (DR)**	**PD62 (DR)**	**PD60**	**PD61**	**PD62**
Total number of aliquots measured					
	48	24	48	48	48
Aliquots rejected for the following reasons					
Poor recycling ratio	2	2	1	0	1
Depletion by IR	32	6	29	29	11
Recuperation	0	0	0	0	0
Saturation/Oversaturation (Approach 3)	0	0	3	3	4
Sum of rejected aliquots					
	34	8	33	32	16
Acceptable individual D_e values					
	14	16	15	16	32

Table S3. Sample depths, water content, and dose rate.

Sample	**Depth below surface (m)**	**Moisture (%)**	**Dose rate (Gy/ka)**			**Total dose rate, (Gy/ka)**
			Beta	*Gamma*	*Cosmic*	
PD60	1.96±0.10	5±2.5	0.09±0.01	0.16±0.01	0.18±0.02	0.44±0.02
PD61	1.02±0.10	5±2.5	0.39±0.03	0.36±0.02	0.20±0.02	0.95±0.04
PD62	0.29±0.10	5±2.5	0.46±0.04	0.36±0.02	0.25±0.02	1.08±0.05

Table S4 Summary OSL dating results and ages.

Sample	**D_b calculation method (n)**	**D_b(Gy)**	**OD (%)**	**Total dose rate, D_r (Gy/ka)**	**Age (ka)**
PD60	CAM (15)	111±10	34±7	0.44±0.02	255±27
PD61	CAM (16)	115±9	28±5	0.95±0.04	121±11
PD62	CAM (32)	121±9	39±5	1.08±0.05	112±10

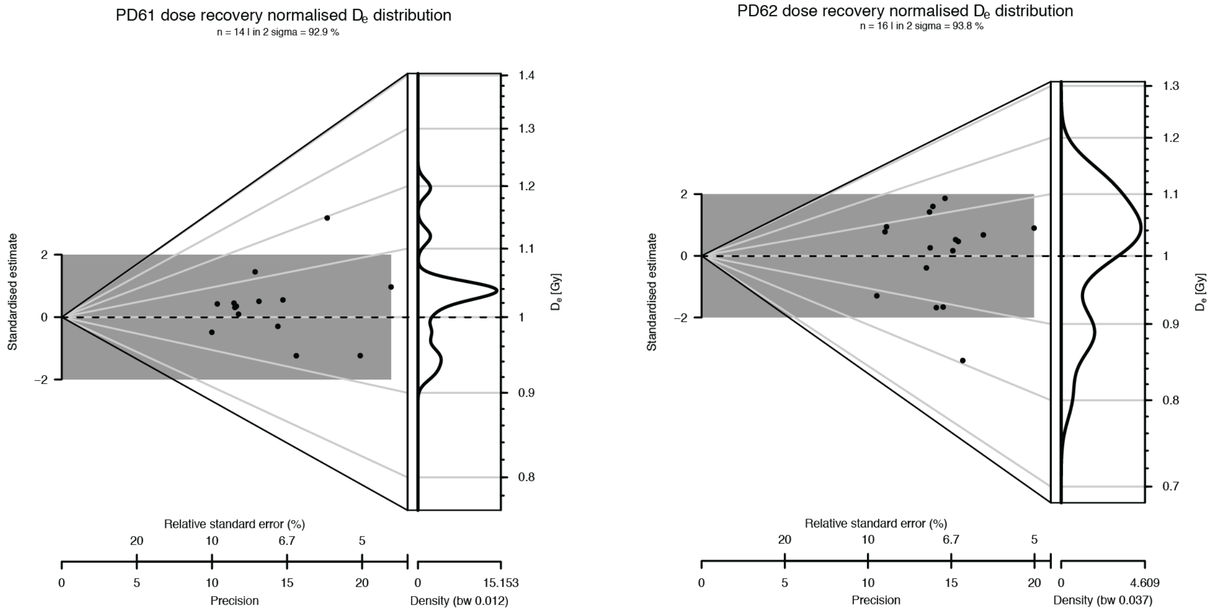

Figure S5. Abanico plots displaying the normalised dose recovery data centred to unity for accepted aliquots with a preheating regime of 200°C held for 10 seconds prior to the measurement of the regenerated dose (L_x) and 160°C held for 5 seconds prior to the measurement of the test dose (T_x). The dose recovery ratio is defined as measured equivalent dose (D_e)/laboratory dose (D_r). See discussion in Supplementary Text 2 for more details.

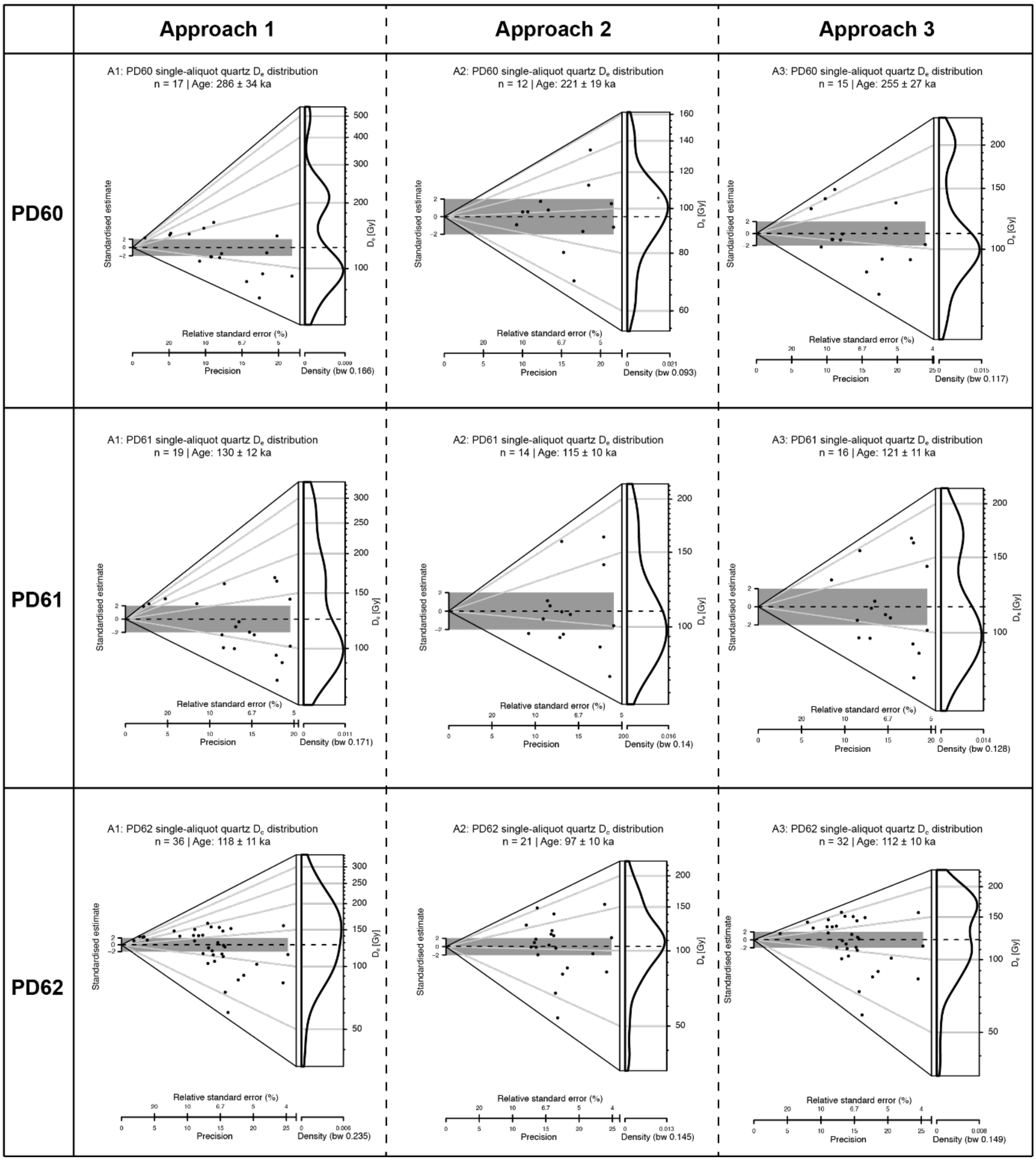

Figure S6. Abanico plots for samples PD60, PD61 and PD62 (top to bottom) for each saturation/oversaturation rejection approach (left to right) (see discussion in Supplementary Text 2). Note that Approach 3 was used to calculate D_b for age determination. The dark grey bar is centred at the CAM D_b (broken black line) and all the points that lie within the bar are consistent (at 2σ) with this dose. Overdispersion values are shown in Table S1 and Table S4 and are discussed in Supplementary Text 2. Abanico plots constructed using the Plot_AbanicoPlot() function in the R luminescence package (*90–91*).

Supplementary Text 3: Electron spin resonance (ESR) and U-series dating

ESR dose evaluation results. Measurement precision achieved is overall excellent, with 4/5 samples showing a variation <1%. This results in a D_E repeatability that is systematically <4%. D_E values appear to be all >1,000 grays (Gy). Consequently, the dose response curve of each sample was restricted to D_{max}/D_E ratios of between 0.9 and 1.8, in accordance with the recommendations by Ref *92* (see Table S6). The five samples display very high D_E values ranging from about 1,100 Gy to 3,100 Gy. These results are lower but nevertheless within the same order of magnitude as the D_E estimates previously obtained for the specimens from TAG locality (3,800-4,500 Gy; *42*), and much higher than that obtained for Al Wusta (<100 Gy; *4*).

Solution U-series analysis. Bulk solution U-series analyses of dental tissues collected from the five tooth samples all return finite U-series age estimates (Table S7). In first instance, these results do not show apparent uranium leaching. These U-series ages are overall quite consistent and range from ca. 243–160 ka. In particular, the enamel tissues from all the teeth vary within narrow range between 174 and 196 ka, suggesting that they may all have experienced the same uptake event. Interestingly, the enamel tissues display very close initial $^{234}U/^{238}U$ ratios (1.81-1.89), much like the dentine tissues (2.01-2.08, excluding #232). The dentine from #232 shows instead a much smaller ratio (1.79), and the most recent apparent U-series age of the data set (~157 ka), suggesting that this dental tissue might have been affected by a recent uranium uptake overprint.

Four of the five teeth (the exception being #232) show a typical delayed uranium uptake in the enamel compared with dentine (i.e., the apparent U-series age of the enamel is younger than that of the dentine), as the result of the significantly slower uranium diffusion rate into this tissue (*93–94*). Consequently, provided that no uranium leaching occurred, the apparent U-series age measured in dentine (ranging from 236–190 ka) may be considered to be a more reliable chronological constraint: they should be interpreted as minimum possible age estimates for the fossils.

Combined U-series and ESR age calculations. U-series analyses show that all enamel tissues display exceptionally high uranium concentration values of up to 70 ppm (Table S7). Beyond 5 ppm of uranium in the enamel, tooth samples are usually considered as being not suitable for combined US-ESR dating (e.g. *95*): calculations typically result in strongly underestimated ages due to the determination of a massively overestimated internal dose rate. Previous works suggested that this is possibly related to an inverse correlation between uranium concentration and alpha efficiency (*96*). In that context, leaving aside sample #2, four of the five teeth appear to be unsuitable for dating purpose. As a matter of fact, none of the combined US-ESR age calculation attempts did return finite estimates. A similar outcome was achieved even when assuming a very rapid uptake with the CSUS model 9 (*55*): the dose generated by dental tissues only is higher than the measured D_E values. Similarly, the use of the AU model (*51*) did not return reliable results. In summary, no existing uranium uptake model used for ESR dating purpose can cope with the present U-series data set.

Sample #2 is perhaps the tooth showing the best potential for US-ESR dating, as it displays the lowest uranium concentration in the enamel of the data set (~5.3 ppm). Still, it does not return any finite US-ESR age estimate. The EU-ESR age of *c.* 101 ka, assuming an Early Uptake (EU = closed system assumption), appears to be significantly younger than the apparent U-series age results. This is usually interpreted as an evidence of uranium leaching (e.g. *97*), suggesting that the U-series age are no longer reliable chronological constraints. This hypothesis should be considered with extreme caution though, as it could simply be the results of an exceptionally massive dose rate associated to dental tissues, which represents 92% of the total dose rate (enamel = 19%, dentine = 10%, cement = 63%). Consequently, the evidence of uranium leaching is not convincingly demonstrated. The presence of a very localized cement layer (about 70–120 um thick) with ~480 ppm of uranium is also an additional complication, as it also generates a massive external beta dose. When not taking into account this cement and considering a sample geometry sediment/enamel/dentine instead, a finite US-ESR age estimate 246±32 ka is obtained, while the CSUS-ESR result is older by about 150 ka. These results are however purely indicative, as the cement is expected to have contributed to 79% to 92% of the external beta dose rate from the outer side of the enamel layer (*98*), which would again not result in the calculation of a finite age. Additionally, when considering sediment sample Ala-SCS instead, the combined US-ESR age gets older by about 7%. The ages presented above should not be considered as reliable chronological constraints for the fossils. These few numbers simply illustrate the significant impact of the exceptional U-series data features displayed by the sample in the dose rate evaluation, which logically result in minimizing the relative weight of other sources of uncertainties, such as the sedimentary environment or the depth of the tooth samples.

Table S5. Details of the fossil teeth sampled for ESR and U-series dating.

Lab code	**Description**	**Provenance**
#2	Oryx left 3rd molar	Surface
#145	Oryx molar	Surface
#188	Med-sized bovid molar	Surface
#228	Med-sized bovid molar	Surface
#232	Med-sized bovid tooth	Surface

Table S6. ESR results derived from the analyses of fossil teeth. Measurement precision is expressed as the mean coefficient of variation obtained for all the aliquots of a given sample after the two or three repeated measurements. D_E precision is the variation of the D_E values derived from the repeated measurements of a given sample. The 1-σ D_E error is a combination of the fitting error and the error on the calibration of the irradiation source (2.3%).

Sample	**Number of repeated measurements**	**Measurement precision (%)**	**D_E precision (%)**	**Adj. r-Square**	**D_E (Gy)**	**Dmax (Gy)**	**D_{max}/D_E**
#2	2	1.4%	0.1%	0.995	1083 ± 84	1502.6	1.4
#145	2	0.3%	1.9%	0.995	2578 ± 179	3005.2	1.2
#188	2	0.4%	0.8%	0.991	3098 ± 290	5008.6	1.6
#228	2	0.3%	1.0%	0.986	2213 ± 240	3005.2	1.4
#232	3	0.7%	3.9%	0.983	1933 ± 191	3005.2	1.6

Table S7. U-series dating results obtained for the five teeth from Alathar. Ratios in parentheses are activity ratios calculated from the atomic ratios. Errors are given at the 2σ level. ^{230}Th ages are calculated using Isoplot EX 3.75 (*175*) with decay constants λ238 = 1.551x10-10 yr-1 (for ^{238}U), λ234 = 2.826x10-6 yr-1 (for ^{234}U) and λ230 = 9.158x10-6 yr-1 (for ^{230}Th), respectively, following Ref *99*.

Sample	**Tissue**	**U (ppm)**	**^{234}U/ ^{238}U**	**^{230}Th/^{232}Th**	**^{230}Th/^{234}U**	**Corrected age (ka)**	**Corrected initial ^{234}U/ ^{238}U**
#2	Enamel	5.4 ± 0.001	1.526 ± 0.001	4033.7	0.882 ± 0.001	186.4 ± 0.6	1.89
#2	Dentine	134.2 ± 0.033	1.629 ± 0.001	40907.8	0.898 ± 0.001	190.5 ± 0.5	2.08
#2	Cement	480.9 ± 0.154	1.488 ± 0.001	6734.8	0.973 ± 0.001	243.3 ± 0.8	1.97
#145	Enamel	69.7 ± 0.023	1.494 ± 0.001	2622.1	0.853 ± 0.001	174.0 ± 0.6	1.81
#145	Dentine	112.7 ± 0.040	1.520 ± 0.001	475.5	0.966 ± 0.002	235.7 ± 1.2	2.01
#188	Enamel	42.4 ± 0.013	1.500 ± 0.001	3612.3	0.894 ± 0.001	193.3 ± 0.8	1.86
#188	Dentine	137.9 ± 0.038	1.590 ± 0.001	4085.7	0.911 ± 0.001	198.7 ± 0.6	2.03
#228	Enamel	52.4 ± 0.021	1.497 ± 0.001	8709.7	0.899 ± 0.001	196.3 ± 0.8	1.86
#228	Dentine	148.0 ± 0.048	1.583 ± 0.001	2826.4	0.926 ± 0.001	207.0 ± 0.8	2.05
#232	Enamel	33.2 ± 0.011	1.503 ± 0.001	2787.0	0.860 ± 0.001	176.7 ± 0.7	1.83
#232	Dentine	84.6 ± 0.037	1.504 ± 0.001	704.5	0.815 ± 0.001	157.8 ± 0.5	1.79

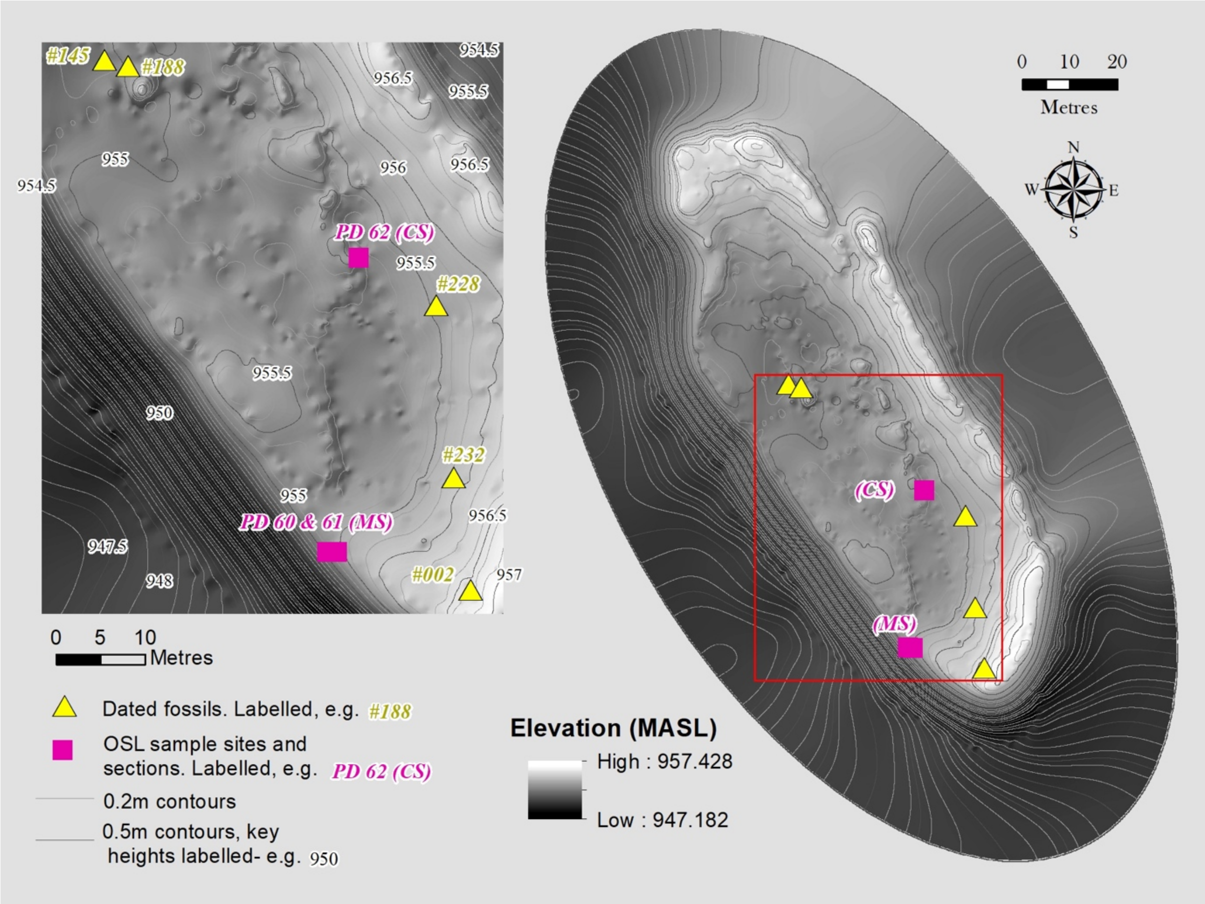

Figure S7. Position of the tooth samples dated by U-series and ESR.

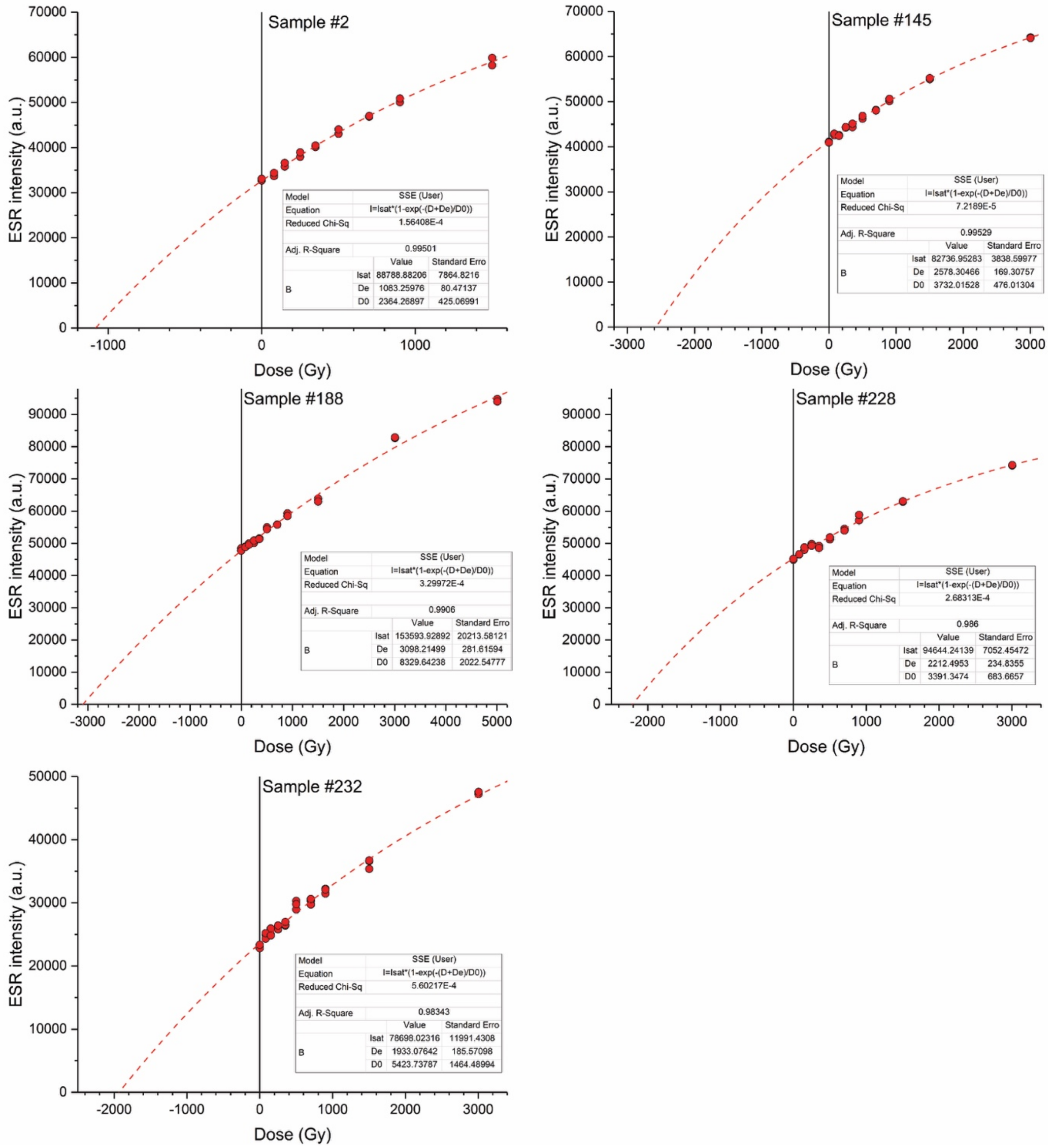

Model	SSE (User)		
Equation	I=Isat*(1-exp(-(D+De)/D0))		
Reduced Chi-Sq	1.56408E-4		
Adj. R-Square	0.99501		
		Value	Standard Erro
B	Isat	88788.88206	7864.8216
	De	1083.25976	80.47137
	D0	2364.26897	425.06991

Model	SSE (User)		
Equation	I=Isat*(1-exp(-(D+De)/D0))		
Reduced Chi-Sq	7.2189E-5		
Adj. R-Square	0.99529		
		Value	Standard Erro
B	Isat	82736.95283	3838.59977
	De	2578.30466	169.30757
	D0	3732.01528	476.01304

Model	SSE (User)		
Equation	I=Isat*(1-exp(-(D+De)/D0))		
Reduced Chi-Sq	3.29972E-4		
Adj. R-Square	0.9906		
		Value	Standard Erro
B	Isat	153593.92892	20213.58121
	De	3098.21499	281.61594
	D0	8329.64238	2022.54777

Model	SSE (User)		
Equation	I=Isat*(1-exp(-(D+De)/D0))		
Reduced Chi-Sq	2.68313E-4		
Adj. R-Square	0.986		
		Value	Standard Erro
B	Isat	94644.24139	7052.45472
	De	2212.4953	234.8355
	D0	3391.3474	683.6657

Model	SSE (User)		
Equation	I=Isat*(1-exp(-(D+De)/D0))		
Reduced Chi-Sq	5.60217E-4		
Adj. R-Square	0.98343		
		Value	Standard Erro
B	Isat	78698.02316	11991.4308
	De	1933.07642	185.57098
	D0	5423.73787	1464.48994

Figure S8. ESR dose response curves obtained for the five tooth enamel samples.

Supplementary Text 4: Chronological considerations

The teeth display unusual U-series data, and in particular very high uranium concentrations in enamel. Because of these features, the samples simply lie beyond the application limits of the combined U-series and ESR dating method. Consequently, the apparent U-series age results are the only direct chronological constraints available for the fossils. The main question is therefore whether this constraint is reliable, or has been biased by uranium leaching.

At face value, the U-series results obtained from bulk samples appear to be overall extremely homogenous and consistent among the samples, suggesting that they reflect the same uranium uptake process. This process took place about 236–190 ka ago, as indicated by the dentine samples. These minimum age constraints for the fossils are older, and therefore in disagreement with, the OSL age results for the Alathar paleolake sediments (OSL samples PD61 and 62). Such a discrepancy could only be explained if the enamel and dentine tissues had been impacted by uranium leaching (thus making the fossils appear older than what they actually are), or if the fossil material was reworked from older, hitherto unknown deposits.

It is difficult to determine definitively whether uranium leaching occurred. If it did, this would imply that at some point in the past, the uranium concentration in dental tissues was even higher than measured today, which seems quite unlikely (although not impossible). The only potential evidence in favour of uranium leaching is given by the ESR dating, and in particular with the calculation of EU-ESR ages that are younger than their U-series equivalents. This is typically interpreted as the result of uranium leaching, but the exceptionally high uranium concentrations measured in the enamel raise some reasonable doubts regarding the reliability of this interpretation. In the absence of spatially-resolved U-series data, no uranium diffusion profiles into dental tissues can be obtained (*93*), which could be another way to identify any potential evidence of uranium leaching in these samples.

In summary, there is no unequivocal evidence suggesting that the dental tissues have experienced uranium leaching, although this hypothesis cannot be discounted. Interestingly, the teeth from TAG locality dated earlier by Ref *42* showed very similar features: very high D_E values (of several thousands of Gy), high uranium concentrations in enamel (between 2 and 61 ppm), and overall consistent U-series ages, and in particular in the enamel (between 270–235 ka), albeit a bit older than those obtained here. Because of the high U concentration in the enamel, only 2/5 teeth from TAG could be tentatively dated by US-ESR. No evidence for uranium leaching was noted for the TAG samples, and the apparent U-series, the combined US-ESR, and the OSL age results were all stratigraphically consistent. At Al Wusta, fossil bone and teeth showed much younger apparent U-series ages and lower uranium concentrations, but again, the different methods, including U-series, provided consistent results (*4*). In other words, in none of the fossil assemblages of the Arabian Peninsula dated until now, have we observed evidence of overestimated apparent U-series age results due to a recent uranium leaching overprint. Consequently, perhaps the most reasonable interpretation that can be derived from the current U-series data set is that the fossil teeth have an age of at least 236–190 ka.

Based on this interpretation, if it is assumed the fossils are coeval with the lake body then that suggests the OSL dates from the paleolake sediment significantly underestimate the true age of the lake deposit. However, there is no evidence that this is the case. The sedimentary environment is ideal for luminescence dating, i.e. sands derived from aeolain/fluvial mobilisation of well-bleached surficial sands and deposited in a shallow waterbody. Overdispersion is relatively high (27–39%) though this likely relates to beta microdosimetry (see SI Text 2) and lies within observed overdispersion values from other luminescence studies within the Nefud (e.g. *11*). Though there were a large number of rejected aliquots, sufficient analysis was carried out on samples directly from the lake sediment (samples PD61 and PD62) to ensure a large number of aliquots passed rejection criteria (PD61 = 16 aliquots, PD62 = 32 aliquots) that could generate robust burial doses. Finally, both ages from the lake sediments are stratigraphically consistent with one another and match a known humid interval in the Arabian Peninsula in MIS 5e. Assuming that both the OSL and U-series datasets are reliable, the most parsimonious conclusion that can be drawn is that the fossil assemblage has been reworked from older deposits, and therefore, pre-date the formation of the footprints.

Physical evidence for the reworking of fossils is difficult to assess here given the clear impact that abrasion by wind-blown sand – and quite possibly salt and insolation weathering – has played in modifying the Alathar fossil assemblage (see SI Text 5). However, the OSL age of the sands that directly underlie the paleolake deposit support the hypothesis that the fossil material has been reworked. These sands date to 255 ± 27 ka and overlap within uncertainties with the U-series dates from the fossils. While this does not imply that the sands and fossils were deposited at the same time, it does suggest that the near surface sands in the immediate vicinity of Alathar prior to the onset of MIS 5e lake development were of a similar age to the fossils. Therefore, these sands may have eroded, yielding fossil material from older humid intervals, which were subsequently deposited into the MIS 5e Alathar waterbody.

It is worth noting that the fossils are similar in overall appearance and are comparable in colour to the paleolake sediments and a number of fossils retained sediment adhered to their cortical surface (SI Text 5). Furthermore, many are manganese stained, indicative of deposition in waterlain sediment. This is not inconsistent with the fossils forming and being deposited within a waterbody during an earlier humid interval, before eroding out and being redeposited in a later lake body. Indeed, many Pleistocene fossils within the western Nefud Desert are presently located on the land surface following deflation of paleolake deposits and dune sands. Were a humid period to occur in the future, these fossils would then be redeposited in later lake bodies.

Finally, it is worth highlighting that the fauna identified from the body fossils are also represented by the footprints (i.e. elephants and medium- and large-sized bovids) (see SI Text 5). This may imply coeval fossilization and formation of the footprints. However, such fauna have repeatedly occupied the western Nefud Desert during episodic humid phases at nearby sites over the past 500,000 years (*4, 25–26, 100*). As such, it remains plausible that some of the fossils represent fauna derived from an older humid interval which have then been reworked, as is suggested by geochronological datasets.

Supplementary Text 5: Fossil and ichnofossil analysis

Fossil taphonomic analysis. In total, 233 specimens were collected and analysed and the full result of the taphonomic analysis, complete skeletal inventory, and list of taxa are provided in Tables S8–S10. While most fossils were loose on the surface, a small number of fossils (*n*=4) were found eroding out of the paleolake sediments and required shallow excavations for their retrieval (Figs. 5J & S11C). The assemblage is dominated by small fragments, most of which fall between 21–50 mm in length (*n*=142, 76%) and 11–30 mm in width (*n*=145, 78%). The abundance of small fossils, coupled with the fact that no additional fossils were found in the days following this initial survey, suggests a comprehensive recovery of surface material at the site. Unweathered specimens are rare (*n*=4, 1.7%) and most can be assigned to weathering stages 1–3 (*n*=137, 58.8%) indicating a slow but eventual burial of bones. Black manganese stained bone (*n*=22, 9.4%) is consistent with deposition in water or damp sediments. A significant number of specimens exhibit pitting and abrasion consistent with abrasion by windblown sands (*n*=100, 42.9%), a process common in desert settings including Arabia (*25*). Furthermore, this suggests that the fossil assemblage, or part thereof, has been sub-aerially exposed for some time. Green-fractured long bones are abundant (*n*=23, 40% of midshafts) and carnivores appear partly responsible, as evidenced by tooth marks on green-fractured bone. That said, tooth-marked specimens are scarce (*n*=6, 3%). This may, however, be largely driven by adhering sediments (*n*=31, 13.3%) and overall poor cortical surface preservation of many of the fossils. Long bones are characterised by shafts that retain less than half their original circumference (*n*=57, 79.2%) and this is probably the result of various post-depositional processes. Post-exhumation processes, such as insolation and salt weathering, may have also contributed to the degradation and fragmentation of the assemblage, as has been suggested for other sites in the Nefud Desert (*25*). Crushed specimens (*n*=18, 7.7%) attest to the assemblage at some point being situated beneath a significant weight of sediment that has since eroded (e.g. lake sediments) or moved (e.g. dune migration).

Systematic paleontology

Order ***Proboscidea*** Iliger, 1811
Family ***Elephantidae*** Linnaeus, 1758
Elephantidae sp.

Description. – Two large enamel fragments (WNEF17_1/217, 230) are consistent with elephantids, but the fragments are small and poorly preserved and provide no further taxonomic insight.

Order ***Artiodactyla*** Owen, 1848
Family ***Bovidae*** Gray, 1921
Genus ***Oryx*** de Blainvill, 1816
Oryx sp.

Description and remarks. – Numerous teeth and tooth fragments resemble those of *Oryx*, with upper molars and premolars having a simple occlusal profile and U-shaped infundibulum. A fragmented upper molar (WNEF17_1/198, 235 [refits]) exhibits a basal pillar that juts lingually before joining the protocone (or metaconule), with the enamel between the two creating a thin oval slit that most closely matches that seen on the second and third upper molars of *O. gazella*, albeit similar features can also occur in other *Oryx* species. An additional poorly preserved upper molar (WNEF17_1/142) is similar in overall appearance and probably represents the same taxon. A partial horn core and parietal bone (WNEF171/218) may also be *Oryx*, but the specimen is distorted and how much of the medio-lateral compression of the horn core is a result of this is difficult to discern.

The extant endemic *O. leucoryx* was abundant in Arabia until relatively recently and *Oryx* fossil remains have been reported from the middle (*25, 42, 100*) and late Pleistocene (*101*) of Arabia, suggesting a long-standing presence in the region. The specimens described here, and possibly much of the medium-sized mammalian post-cranial material recovered from the site, can probably be referred to *Oryx*.

Small Bovidae gen. et sp. indet.

Description. – Two small bovid metapodial shaft fragment (WNEF17_1/22, 119) represent at least one other smaller bovid at the site.

cf. large Bovidae gen et sp. indet.

Description. – A large proximal (or intermediate) phalanx (WNEF17_1/153), preserving the distal epiphysis and diaphysis, is provisionally referred to a large Bovidae. The specimen is poorly preserved, exhibits significant cortical exfoliation and exposure of cancellous bone, and is slightly distorted.

Brief background on experimental track studies. Ichnology is the study of fossilized tracks (e.g. footprints) and other traces. Tracks and trackways (that is, prints and sets of prints generated by an individual) provide unique opportunities to investigate locomotion, behaviour, and hominin-animal-environment interactions across very short time intervals (e.g. *7*). The taphonomic factors affecting the long-term preservation of tracks means that groups of stratigraphically associated tracks, and particularly those in similar states of preservations, can be assumed to have been generated within a very short window, usually within a few hours or days (*7, 9*). An experimental study of modern human footprints in mud flats found that fine details were lost within two days and prints were rendered unrecognisable within four (*7*), and similar observations have been made for other non-hominin mammal tracks (*9*). Physical variables mediating track formation and preservation include substrate properties (e.g. grain size, water content), erosion, desiccation, precipitation, and compaction, while biological variables include body mass, behaviour, trampling, and bioturbation (see Refs *9, 58* for detailed discussion on the physical and biological processes affecting track formation and preservation). Tracks in circum-lacustrine settings, which are common in the ichnofossil record due to the conduciveness of fine-grained muddy sediments for track formation, are further subjected to seasonal lake level fluctuations, daily wave and sieche action, repeated desiccation events, and microbial mat development (i.e., sheets of bacteria and/or archaea that develop within prints) (*9*). Following exhumation, tracks undergo rapid degradation resulting in their swift removal from the ichnofossil record (*102–104*). Considering the suite of independent and interactive processes affecting the long-term preservation of tracks, it should come as no surprise that they are rarely preserved in the geological record.

Hominin track-bearing sites are especially rare, and those dating to the Plio-Pleistocene number less than 40 (see Ref *105* Table S1). Nonetheless, they have provided remarkable insights into hominin locomotion and behavior that cannot be gleaned from archaeological and fossil records alone. Here we provide just some examples of the significant insights studies of hominin footprints have provided.

The Laetoli Bed footprints at Laetoli, Tanzania, provided the earliest definitive evidence for bipedal locomotion among Pliocene hominins (*106–109*). The Ileret footprints, Kenya, demonstrated that by 1.5 million-years-ago *Homo erectus* had developed a foot form and gait comparable to *H. sapiens* (*110–111*). Hominin prints were found to be disproportionately abundant at Ileret, suggesting intensive use of the lake margin habitat (*7, 112*). Moreover, these tracks have been interpreted as multi-male groups moving in concert through the landscape, providing credible evidence for labor division and male-male cooperative behavior among early Pleistocene hominins (*7–8*). Footprints dated to *c.* 700 ka at the site of Gombore II-2, Ethiopia, document the repeated use of the lake margin by adults and children over a very short time, probably within a single season (*113*). Those tracks, coupled with onsite evidence for carcass butchery, suggest mixed-aged family groups were cooperatively foraging at the site (*113*). Webb and colleagues (*114*) made similar observations from the adult and juvenile late Pleistocene *H. sapiens* footprints at Willandra Lakes, Australia. More recently, a study of a large sample of *H. neanderthalensis* footprints from Le Rozel, France, found that the group probably comprised of between 10 to 13 people, most of which were children (*105*). In White Sands National Monument, USA, a series of prints document the stalking/hunting of giant ground sloth by late Pleistocene humans (*115*). Tracks and trackways have therefore shown great potential for providing unique insights into various aspects of early hominin life, particularly for understanding their social structure and behavior.

Systematic ichnology

Ichnogenus ***Proboscipeda*** Panin and Avram, 1962
Proboscipeda isp.

Description. – Large, circular to near-circular tracks (*n*=43), preserved as concave epirelief impressions in the paleolake sediment, are clearly attributable to a proboscidean (Fig. 5D, E). Tracks are typically longer than they are wide, but some have a width equal to length. Track length varies greatly, with diameters ranging from 190–630 mm, indicating the presence of a herd consisting of both adults and juveniles. Displacement rims and radial fractures were common and often encompassed the track. Toe impressions and overprinting were rarely observed. Load deformation was clearly visible in one of the prints where the paleolake sediment had broken off, exposing the print cross-section (Fig. S11D).

Remarks. – The lack of toe impressions and a length exceeding the width is consistent with *Pro. enigmatica*, the type ichnospecies for the ichnogenus *Probosciepda* (*116*). The Alathar prints are, however, larger than the range reported for this ichnospecies (420–520 mm) and are more comparable in size to prints attributed to *Pr. panfamilia* (*117*). However, *Pro.*

panfamilia often exhibit toe impressions and forefoot overprinting (*117–119)*, features which are mostly absent in the Alathar tracks. The Alathar tracks are therefore referred to the inchogenus *Proboscipeda*.

The larger Alathar track lengths far exceed those of the extant African *Loxodonta africana* (170–530 mm, *n*=30) and Asian *Elephas maximus* (370–400 mm, *n*=2) (data from Refs *120–121*). The extant African elephants may also be discounted as possible trackmakers on the basis of their late Pleistocene fossil record, which, like their present-day distribution, is restricted to sub-Saharan Africa (*122*).

During the late Pleistocene, proboscideans were far more diverse and widespread, and many species far exceeded the size of the extant elephants. The large grassland-adapted *Palaeoloxodon iolensis*, considered by some to represent the terminal subspecies of the *Pal. recki* lineage, may have persisted in North Africa until *c.* 35 ka (*122–123*). Various large proboscideans (e.g. *Pal. antiquus*, *M. primigenius*) occupied parts of Europe up until the end of the late Pleistocene/early Holocene, but their ranges appear to have been restricted to the more northerly latitudes (*124–125*). Proboscidean remains are notably scarce in southwest Asia from *c.* 400 ka onwards, possibly due to an increase in hominin hunting pressures in the region (*24*). The findings presented here are therefore of considerable interest. *Palaeoloxodon antiquus* remains recovered from Holon, Israel, may date to as young as *c.* 200 ka (*126*), but other researchers have questioned the validity of these dates, suggesting that fossil remains are in fact much older (*c.* 500 ka) (*24, 127*). More recently, remains tentatively attributed to *Pal. recki*, dated to *c.* 266 ka and *c.* 125 ka, were discovered at Shishan Marsh, Jordan (*128*). Unstratified remains provisionally attributed to *E. hysudricus*, but likely originating from the same layers, were also recovered at the site (*128*). Other provisionally identified remains of *E. hysudricus* were also discovered at the nearby sites of Ma'ayan Baruch and 'Ain Soda, Israel, and dated to *c.* 500–220 ka (*129*). While it remains difficult to speculate as to the trackmaker at Alathar, it seems likely that is was a large-bodied grassland adapted elephant (e.g. *Pal. recki*).

Ichnogenus ***Hippipeda*** Vyalov, 1965
Hippipeda isp.

Description. – A single digit impression (digit III) with a hemi-ellipsoidal/arrowhead outline that is tapered to the anterior (WNEF17_1/PR158; Fig. 5I). The track is widest towards the posterior and the margins of the posterior end of the track run roughly parallel. The two posterior bars connect and isolate the sole (following Ref *118*). Greatest length and width measure 70 mm and 60 mm, respectively.

Remarks. – The Alathar print closely resembles those attributed to *Hip. cardstoni* from Walley's beach in Canada but is shorter than the range reported for this ichnospecies (90–120 mm) (*118*). Given that only a single print is present at Alathar, we refer it to the ichnogenus *Hippipeda.*

Equids are relatively common in the Arabian Pleistocene fossil record (*26*). Remains of *E. hemionus* have been recovered from the nearby site of Ti's al Ghadah (*42*) and provisionally assigned remains from southern Arabia (*101, 130*). Remains of larger equids are also known from numerous Pleistocene sites in the Nefud Desert (*25, 42*). The size of the Alathar track falls below those reported for African zebra in tracking guides (c.f. Refs *131–132*), suggesting perhaps one of the smaller wild asses (e.g. *E. hemionus*), although it's possible that the trackmaker was a juvenile.

Ichnogenus ***Lamaichnum*** Aramayo and Branco, 1987
Lamaichnum isp.

Description. – Bidigital, digitigrade tracks with rounded anterior ends and lacking claws (*n*=107). Anterior digits rarely convergent and are typically parallel. Posterior end wider than anterior and particularly so for the forefoot. Hindfoot tracks ovoid in outline (Fig. 5H), whereas forefoot tracks are more triangular/heart-shaped, tapering to the anterior (Fig. 5G). Both forefoot and hindfoot impressions exhibit a posterior gap and a medial pocket was occasionally observed. Tracks vary in length from 80–240 mm, indicating the presence of both juveniles and adults.

Remarks. – Broadly, the shape and size of the Alathar prints resembles *L. sarjeanti* but differ in that the length typically exceeds the width, whereas in *L. sarjeanti* the length and width are approximately equal (*118*). In this regard, the Alathar prints are more similar to *L. macropodum*, but lack claw marks often associated with this ichnospecies (*118*). The lack of this feature may, however, be due to wind abrasion.

The Pleistocene camelid fossil record of Africa and Eurasia is scant, and most fossils are too poorly preserved to be adequately described. As a result, our understanding of the biogeographical history of *Camelus* remains patchy and the relationship between identified species unclear. In Arabia, remains of a large *Camelus* were recovered from the western Nefud Desert and dated to *c*. 500–300 ka (*42, 133*) and rock art depictions indicate the presence of wild camels in the region during the early Holocene (*134*). Given that camels are well-suited to arid environments, it's possible that they have had a long-standing presence in the Arabian Peninsula from as early as the middle Pleistocene, and perhaps even earlier, making speculation about the specific trackmaker of the Alathar prints difficult.

Ichnogenus ***Bijugopeda*** Sarjeant and Reynolds, 1999

Bijugopeda isp.

Description. – A single large bidigital, digitigrade footprint with two separate kidney bean-shaped toe impressions is clearly that of a large bovid (WNEF17_1/070; Fig. S11A). The anterior and posterior ends taper inwards producing a medial pocket that is widest in the centre of the track. Greatest length and width measure 140 mm and 190 mm, respectively. The greater width, coupled with the tapered anterior and posterior ends, produces a track that is oval in outline. Another large ovoid track with a broadly similar outline may represent a second track but it is too poorly preserved to be certain.

Remarks. – The shape and size of the Alathar track closely matches those attributed to *Bijugopeda anterofossa* from Walley's Beach in Canada suggested to have been produced by the large extinct *Bison antiquus* (*118*). It differs in its overall shape, as well as in its much greater length and width, to tracks produced by alcelaphines (e.g. *Alcelaphus*) and hippotragines (e.g. *Oryx*), as displayed in various tracking guides (e.g. Refs *131–132*). Considering this, and the fact that *Syncerus* is the only large bovid known from the western Nefud Desert during the Pleistocene (*25–26*), it seems reasonable to suggest that *Syncerus* is the likely trackmaker at Alathar.

Ichnogenus ***Pecoripeda*** Vyalov, 1965

cf. *Pecoripeda* isp.

Description. – A medium-sized bidigital, digitigrade track (WNEF17_1/205; Fig. S11B) with convex lateral margins giving the track and ovoid outline. Length and width measure 60 mm and 70 mm, respectively, with the widest point of the track being across its centre. The track exhibits claw impressions, as well as shallow posterior and anterior gaps, but lacks a medial pocket. A second similar, albeit slightly distorted, print was found adjacent to this print and probably represents the same individual (WNEF17_1/204). Given the relative positions of the prints, the individual appears to have been stationary.

Remarks. – The Alathar tracks differ from most *Pecoripeda* tracks in their oval outline and being wider at the middle as opposed to the heel (see Ref *135*). In this latter feature, they resemble *Pecoripeda djali* but differ again in being wider than they are long and with less discernible toe impressions. The Alathar tracks are tentatively referred to the ichnogenus *Pecoripeda*, but do not resemble, to the best of our knowledge, any described *Pecoripeda* ichnospecies. It is possible that wind abrasion has drastically altered the morphology of the print. Indeed, Ref *103* found tide action significantly and rapidly altered the morphology of ungulate tracks following exposure (see also Ref *104*). For example, they found that the borders of some ungulate prints went from being undercut at the start of the experiment to be shallow and slanted within just four days.

Ichnogenus ***Hominipes*** Kim et al., 2008
Hominipes modernus Kim et al., 2008

Description. – Plantigrade tracks with a pronounced medial longitudinal arch, abducted hallux, rounded digit and heel impressions, and a wide metatarsal region (n=7). In some cases, the heel, medial metatarsal heads, and hallux are most strongly impressed, reflecting medial weight transfer during bipedal locomotion. Length (Heel–D2) and ball width (B1–B2) ranged from 247–292 mm (mean = 262 mm) and 100–130 mm (mean = 116 mm), respectively. An additional four prints are provisionally referred to *Hominipes* as they are of a consistent size and shape, but lack fine details required for positive identification

Remarks. – To date, only two hominin ichnotaxa have been formally described – *Praehominipes laetoliensis* (*136*) and *Hominipes modernus* (*137*). The Alathar tracks clearly differ from those of *Pra. laetoliensis* (based and named after the Laetoli trackways) in their large size and differences in morphology, in particular their rounded heel, prominent and well-defined ball and instep regions, and fixed longitudinal arch. The Alathar prints are consistent in both size and morphology with *Hom. modernus* and for reasons discussed here, as well as in the main article, it is argued that *Homo sapiens* was the probable trackmaker.

Both *H. sapiens* and *H. neanderthalensis* are known from the immediately adjacent Levant during the late Pleistocene but their occupation of the region appears to have been largely asynchronous (*20*). *Homo sapiens* appeared in the Levant during the warm and humid last interglacial, as represented by the dozens of individuals recovered from Skhul and Qafzeh (*6*), and recent findings from the Levant (*3*) and Greece (*2*) suggest an even earlier, middle Pleistocene dispersal. *Homo sapiens* dispersed into the Arabian interior by ~85 ka, as evidenced by a fossil finger bone recovered from Al Wusta, a site just 11 km south of Alathar (*4*). Numerous Middle Paleolithic stone tool assemblages, some of which have been provisionally attributed to *H. sapiens* based on similarities with Levantine and African MIS 5 toolkits, have been recovered from the western Nefud Desert (*16, 19*), as well as further east and south (*15, 17, 138*). Consequently, it appears that *H. sapiens* was geographically widespread in Arabia during MIS 5. In contrast, *H. neanderthalensis* seems to have been absent from the Levant during this period and only appears alongside the arrival of the cold and arid MIS 4 (*20*). The Tabun 1 *H. neanderthalensis* individual – excavated nearly 100 years ago – is the one possible exception to this pattern, but its exact provenance remains unknown (*139–140*), radiometric dating results have varied widely (*141–142*), and its precise taxonomy continues to be debated (Ref *143* and references therein). Therefore, it seems *H. sapiens* is the most likely candidate for the Alathar hominin tracks. This is further supported by the stature and mass estimates, which are more consistent with those of early *H. sapiens* than *H. neanderthalensis* (see below).

Hominin track assemblage analysis. Four prints (HPR001–004) were found adjacent to one another along the south-western edge of the paleolake exposure (Fig. 1), and given their similar orientation, distances from one another, and differences in size (Table S11), are interpreted as two, or up to three, individuals travelling together. The remaining three prints, and four tentatively attributed to *Hominipes*, are scattered across the paleolake deposit.

Print morphometric data was compared to modern human footprints generated under experimental settings, as well as large print assemblages attributed to Pleistocene and Holocene hominins (Table S12). Mean print length is closest to that of the late Pleistocene *Homo sapiens* from Willandra Lakes, Australia (difference [Δ] = 0.1 cm) (*114, 146*), followed by modern unshod Daasanch sample (Δ = 0.8 cm) (*59*), while mean print width is identical to the modern unshod Indian sample (Δ = 0.0 cm) (*144*). The Alathar prints are comparatively broad with a footprint index (FPI) closest to the *H. neanderthalensis* Le Rozel (Δ = 0.00) (*105*) and the modern unshod Indian (Δ = 0.03) samples. It should be noted, however, that footprint morphometry can vary significantly within a population (*59, 144*) and even within an individual trackway (*145–146*). Post-exhumation processes (e.g. wind erosion, tide action) may further alter print size and morphology and, as a result, amplify the variation within in a track assemblage (*103–104*). For example, Ref *103* found an increase in footprint length of as much as 6% as a result of lake tides acting on tracks. As such, any extrapolations based on footprint size or morphology should be considered with caution. Still, we present the speed, stature, and mass estimates below, and compare these to estimates for early *H. sapiens* and *H. neanderthalensis* based on allometric relationships between bone size – primarily limb bone length – and body height and mass (Table S14–S15; Fig. S10).

Speed estimates obtained for the only identifiable stride in the Alathar assemblage (i.e. HPR001 and HPR003) returned values around the expected transition from walking to running (~2.2 m/s) (*58–59*). Therefore, the "walk and run" regression equation was selected to estimate stature (eqn 2) and body mass (eqn 3) of the Alathar printmakers, and these results reported in Table S13.

$$\text{Stature}_{\text{walk \& run}} = 73.29 + 3.78*\text{FPL} \pm 5.4 \qquad [2]$$

$$\text{Mass}_{\text{walk \& run}} = 3.94 + 1.87*\text{FPL} \pm 3.70 \qquad [3]$$

Stature estimates for the Alathar hominins ranged from 166–182 cm with a mean (172 cm) closest to that of the Daasanach and estimates for early *H. sapiens* (Fig. S10A). Mass estimates ranged from 53–67 kg with a mean (58 kg) closest to those for the modern Daasanch people (Fig. S10B). When stature and mass are plotted together, the Alathar prints fall within the estimates of *H. sapiens* but outside those for *H. neanderthalensis* (Fig. S10C).

Table S8. Results of the taphonomic analysis

		Small mammals	**Medium mammals**	**Large mammals**	**Indet. mammals**	**Total**
Midshaft breakage						
Green	*n*	4	23	-	-	27
Dry	*n*	1	12	-	1	14
Both	*n*	2	15	-	1	18
Circ. completeness						
Type 1	*n*	7	48	-	2	57
Type 2	*n*	-	3	-	-	3
Type 3	*n*	1	9	1	1	12
Weathering						
0	*n*	1	1	-	2	4
1	*n*	1	31	-	3	35
2	*n*	2	48	-	6	56
3	*n*	3	34	1	8	46
4	*n*	-	5	-	1	6
Indet.	*n*	4	63	1	18	86
Crushing	*n*	1	14	-	3	18
	%	9.1%	11.3%	0.0%	8.3%	13.1%
Gnawing	*n*	-	7	-	-	7
	%	0.0%	5.6%	0.0%	0.0%	4.0%
Abrasion/rounding	*n*	8	76	-	16	100
	%	72.7%	41.8%	0.0%	42.1%	42.9%
Manganese staining	*n*	2	18	-	2	22
	%	18.2%	14.5%	0.0%	5.6%	12.7%
Adhering sediment	*n*	1	26	-	4	31
	%	9.1%	21.0%	0.0%	11.1%	17.9%

Table S9. Complete skeletal inventory (NISP)

	Small mammal	**Medium mammal**	**Large mammal**	**Indet. mammal**	**Total**
NRSP	11	182	2	38	233
NISP	11	124	2	36	173
Horn core	-	3	-	-	3
Crania	-	7	-	-	7
Maxilla	1	-	-	-	1
Mandible	-	4	-	-	4
Isolated tooth	-	16	1	-	17
Atlas	-	1	-	-	1
Axis	-	1	-	-	1
Thoracic vertebra	-	1	-	-	1
Indeterminate vertebra	-	1	-	-	1
Rib	-	4	-	-	4
Scapula	1	2	-	-	3
Pelvis	-	1	-	-	1
Humerus	1	5	-	-	6
- Prox. ep.	-	-	-	-	-
- Prox. ep. + shaft	-	-	-	-	-
- MSHF	1	3	-	-	4
- Dist. ep. + shaft	-	2	-	-	2
- Dist. ep.	-	-	-	-	-
Radius	1	2	-	-	3
- Prox. ep.	-	1	-	-	1
- Prox. ep. + shaft	-	1	-	-	1
- MSHF	1	-	-	-	1
- Dist. ep. + shaft	-	-	-	-	-
- Dist. ep.	-	-	-	-	-
Femur		1	-	-	1
- Prox. ep.	-	-	-	-	-
- Prox. ep. + shaft	-	-	-	-	-
- MSHF	-	-	-	-	-
- Dist. ep. + shaft	-	1	-	-	1
- Dist. ep.	-	-	-	-	-
Tibia	-	2	-	-	2
- Prox. ep.	-	-	-	-	-
- Prox. ep. + shaft	-	-	-	-	-
- MSHF	-	1	-	-	1
- Dist. ep. + shaft	-	-	-	-	-
- Dist. ep.	-	1	-	-	1
Metatarsal	-	3	-	-	3
- Prox. ep.	-	2	-	-	2
- Prox. ep. + shaft	-	1	-	-	1
- MSHF	-	-	-	-	-
- Dist. ep. + shaft	-	-	-	-	-
- Dist. ep.	-	-	-	-	-
Metapodial	1	9	-	-	10
- Prox. ep.	-	-	-	-	-
- Prox. ep. + shaft	-	-	-	-	-
- MSHF	1	4	-	-	5
- Dist. ep. + shaft	-	4	-	-	4
- Dist. ep.	-	1	-	-	1
Phalanx	-	3	1	-	4
Midshaft fragment	6	58	-	2	66
Unidentified	-	58	-	36	94

Table S10. Fossil and ichnofossil taxa represented at Alathar (taxa listed in parentheses are probable trackmakers).

Taxon	**Fossil**	**Ichnofossil (prints)**
Elephantidae sp.	x	
Proboscipeda isp. (*Palaeoloxodon* sp.)		x
Hippipeda isp. (*Equus* sp.)		x
Oryx sp.	x	
Lamaichnum isp. (*Camelus* sp.)		x
Bijugopeda isp. (*Syncerus antiquus*).		x
Pecoripeda isp. (medium-sized bovid)		x
Small bovid gen. et sp. indet	x	
cf. large bovid gen. et sp. indet	x	
Hominipes modernus (*Homo sapiens*)		x

Table S11. Alathar hominin track morphometric data (cm) following Fig. S9A.

Track	**Side**	**Heel–Hallux**	**Heel–D2**	**Heel–D3**	**Heel–D4**	**Heel–D5**	**B1–B2**	**H1-H2**	**I1-I2**
HPR001	R	28.8	29.2	28.9	28.7	27.8	13.0	7.0	6.0
HPR002	R	24.6	25	24	22	21.5	13.0	5.8	7.0
HPR003	R	28.6	29	-	-	-	12.0	7.5	5.5
HPR004	R	26.5	27	25.5	24	22	10.0	6.5	5.5
HPR005	L	24.8	25.8	-	-	-	10.5	6.6	-
PR212	R	-	-	22.8	22.3	20.8	-	5.4	-
PR347	L	23.9	24.7	-	-	-	11.1	5.9	3.8

Table S12. Footprint length, breadth and index values compared to those of modern humans and various fossil hominin track assemblages. Taxa listed in parentheses are suspected trackmakers.

Site	**Footprint length (cm)**		**Footprint breadth (cm)**		**FPI**	**Reference**
	Mean	Range (s.d.)	Mean	Range (s.d.)		
Modern Human (Daasanach, Kenya)	25.4 (*n*=41)	20.0–29.5 (2.1)	9.7 (*n*=41)	7.4–11.8 (0.9)	0.38	*59*
Modern Human (India)	24.9 (*n*=168)	22.4–28.0 (1.4)	11.6 (*n*=162)	9.2–13.8 (1.3)	0.47	*144*
Walvis Bay (Holocene *H. sapiens*)	22.8 (*n*=87)	19.6–26.1 (1.7)	8.7 (*n*=83)	5.0–11.0 (0.9)	0.38	*145*
Willandra Lakes* (Late Pleist. *H. sapiens*	26.1 (*n*=16)	24.0–30.0 (1.9)	9.6 (*n*=7)	9.0–10.0 (0.3)	0.37	*114, 146*
Le Rozel** (*H. neanderthalensis*)	21.5 (*n*=22)	18.0–28.4 (2.9)	9.5 (*n*=59)	6.9–12.8 (1.4)	0.44	*105*
Roccamonfina (*H. heidelbergensis*)	24 (*n*=56)	-	10 (*n*=56)	-	0.41	*147*
Happisburgh (*H. antecessor*)	19.1 (*n*=12)	14.0–26.0 (4.2)	7.5 (*n*=12)	5.0–11.0 (1.8)	0.39	*102*
Ileret (*H. erectus*)	25.3 (*n*=28)	20.5–30.5 (2.2)	9.6 (*n*=36)	7.5–12.7 (1.2)	0.38	*110*
Alathar **(late Pleist. *H. sapiens*)**	**26.2** **(n=6)**	**23.9–28.8** **(2.1)**	**11.6** **(n=6)**	**10.0–13.0** **(1.2)**	**0.44**	**This study**

* Averaged adult trackway values (*114, 146*); ** Subset of individuals with footprint length greater than 18 cm (following Ref *105*)

Table S13. Stature and mass estimates for the Alathar prints using the 'walk and run' linear fit equations from Ref *59*.

Print	**Stature (cm)**	**Mass (kg)**	**Speed (m/s)**
HPR001	182.15	57.80	2.99
HPR002	166.28	49.94	-
HPR003	181.40	57.42	2.99
HPR004	173.46	53.50	-
HPR005	167.03	52.82	-
PR212	-	-	-
PR347	163.63	53.40	-

Table S14. Stature estimates of late Pleistocene *H. sapiens* and *H. neanderthalensis*.

Site	Assigned taxon	Sex	Stature (cm)	Element of estimate	Refs
Abri Pataud 1	*H. sapiens*	Female	162.2	Upper limb long bone	*148*
Baousso de Torre 1	*H. sapiens*	Male	189.6	Femur	*149*
Baousso de Torre 2	*H. sapiens*	Male	182.5	Femur	*149*
Barma Grande 1	*H. sapiens*	Male	189	Femur	*149*
Barma Grande 2	*H. sapiens*	Male	179.4	Femur	*149*
Barma Grande 5	*H. sapiens*	Male	180.4	Femur	*149*
Bruniquel 24	*H. sapiens*	Male	158.4	Femur	*149*
Cap Blanc	*H. sapiens*	Female	161	Femur	*149*
Caviglione I	*H. sapiens*	Male	174.6	Femur	*149*
Chancellade	*H. sapiens*	Male	160.2	Femur	*149*
Combe-Capelle	*H. sapiens*	Male	163.7	Femur	*149*
Cro-magnon 1 (CM-1)	*H. sapiens*	Male	172.1	Lower and upper limb long bone	*148*
Cro-magnon 3	*H. sapiens*	Male	178.1	Femur	*149*
Cro-magnon 4293	*H. sapiens*	Indet.	173.8	Upper limb (long bone)	*148*
Cro-magnon 4297	*H. sapiens*	Indet.	178.0	Upper limb (long bone)	*148*
Cro-magnon 4322	*H. sapiens*	Indet.	178.9	Upper limb (long bone)	*148*
Cro-magnon 4324	*H. sapiens*	Indet.	160.0	Upper limb (long bone)	*148*
Cro-magnon 4330	*H. sapiens*	Indet.	173.7	Upper limb (long bone)	*148*
Cro-magnon 4337	*H. sapiens*	Female	170.2	Lower limb (foot bone)	*148*
Cro-magnon 4345	*H. sapiens*	Indet.	171.9	Lower limb (foot bone)	*148*
Cro-magnon 4345-Bis	*H. sapiens*	Indet.	170.6	Lower limb (foot bone)	*148*
Cro-magnon 4346	*H. sapiens*	Indet.	169.6	Lower limb (foot bone)	*148*
Cro-magnon 4347	*H. sapiens*	Indet.	169.8	Lower limb (foot bone)	*148*
Cro-magnon 4348	*H. sapiens*	Indet.	170.0	Lower limb (foot bone)	*148*
Dolní Věstonice 13	*H. sapiens*	Male	171.6	Lower and upper limb (long bone)	*148*
Dolní Věstonice 14	*H. sapiens*	Male	185.0	Lower and upper limb (long bone)	*148*
Dolní Věstonice 15	*H. sapiens*	Male	160.1	Lower and upper limb (long bone)	*148*
Dolní Věstonice 16	*H. sapiens*	Male	174.2	Lower and upper limb (long bone)	*148*
Dolní Věstonice 3	*H. sapiens*	Female	163.4	Lower and upper limb (long bone)	*148*
Gough's Cave 1	*H. sapiens*	Male	168.0	Lower limb (long bone)	*148*
Grotte des Enfant 4	*H. sapiens*	Male	186.9	Femur	*149*
Grotte des Enfant 5	*H. sapiens*	Female	164.6	Femur	*149*
Klasies River (Mt I)	*H. sapiens*	Male	164.1	Lower limb (foot bone)	*148*
Klasies River (Mt II)	*H. sapiens*	Indet.	178.6	Lower limb (foot bone)	*148*
La Madelaine	*H. sapiens*	Female	171.6	Femur	*149*
Minatogawa 1	*H. sapiens*	Male	152.9	Lower and upper limb (long bone)	*148*
Minatogawa 2	*H. sapiens*	Female	144.8	Lower and upper limb (long bone)	*148*
Minatogawa 3	*H. sapiens*	Female	149.3	Lower and upper limb (long bone)	*148*
Minatogawa 4	*H. sapiens*	Female	147.7	Lower and upper limb (long bone)	*148*
Minatogawa Q	*H. sapiens*	Indet.	162.1	Lower limb (foot bone)	*148*
Mirón 1	*H. sapiens*	Female	160.7	Lower limb (foot bone)	*148*

Table 14. *Continued.*

Site	Assigned taxon	Sex	Stature (cm)	Element of estimate	Refs
Mladeč 24	*H. sapiens*	Indet.	191.6	Upper limb (long bone)	*148*
Mladeč 27	*H. sapiens*	Indet.	176.9	Lower limb (long bone)	*148*
Mladeč 30	*H. sapiens*	Indet.	173.3	Long limb (foot bone)	*148*
Obercassel 1	*H. sapiens*	Male	168.5	Femur	*149*
Obercassel 2	*H. sapiens*	Female	163.6	Femur	*149*
Ohalo 2	*H. sapiens*	Male	175.0	Lower and upper limb (long bone)	*148*
Omo Kibish 1	*H. sapiens*	Female?	163.3	Lower limb (long bone)	*148*
Paglicci 25	*H. sapiens*	Female	170.4	Lower and upper limb (lone bone)	*148*
Paglicci I	*H. sapiens*	Male	170.4	Femur	*149*
Paviland I	*H. sapiens*	Male	176	Femur	*149*
Pavlov 1	*H. sapiens*	Indet.	186.3	Lower and upper limb (long bone)	*148*
Predmost 10	*H. sapiens*	Male	157.9	Femur	*148*
Predmost 14	*H. sapiens*	Female	169.7	Femur	*148*
Predmost 4	*H. sapiens*	Male	160.6	Femur	*148*
Predmost 9	*H. sapiens*	Female	169.2	Femur	*148*
Předmostí 1	*H. sapiens*	Female	153.7	Lower limb (long bone)	*148*
Předmostí 3	*H. sapiens*	Male	182.0	Lower and upper limb	*148*
Qafzeh 3	*H. sapiens*	Female	164.8	Lower limb (long bone)	*148*
Qafzeh 7	*H. sapiens*	Female	171.8	Ulna	*150*
Qafzeh 8	*H. sapiens*	Male	192.7	Humerus	*150*
Qafzeh 9*	*H. sapiens*	Female	172.5	Lower and upper limb (long bone)	*148*
Skhul 3	*H. sapiens*	Male	180.6	Lower limb	*148*
Skhul 6	*H. sapiens*	Male	177.9	Lower limb	*148*
Skhul IV*	*H. sapiens*	Male	181.85	Upper and lower limb (long bone)	*150*
Skhul V*	*H. sapiens*	Male	194.4	Humerus	*150*
Skhul VII	*H. sapiens*	Female	157	Ulna	*150*
St Germain la Rive	*H. sapiens*	Female	158.1	Femur	*149*
Sunghir 1	*H. sapiens*	Male	183.6	Lower and upper limb (long bone)	*148*
Tagliennte	*H. sapiens*	Male	165.5	Regression from femur measurements	*149*
Tianyuan 1	*H. sapiens*	Indet.	171.9	Lower limb (foot bone)	*148*
Veneri 1	*H. sapiens*	Male	177.1	Lower limb (long bone)	*148*
Veneri 2	*H. sapiens*	Female	173.2	Lower limb (long bone)	*148*
Veryier	*H. sapiens*	Male	172	Femur	*149*
Amud 1*	*H. neanderthalensis*	Male	176.8	Lower limb (long bone)	*150*
Feldhofer	*H. neanderthalensis*	Indet.	165.6	Lower and upper limb (long bone)	*150*
Kebara 2*	*H. neanderthalensis*	Male	172	Lower and upper limb (long bone)	*150*
Kebara 9	*H. neanderthalensis*	Female	158	Lower limb (foot bone)	*148*
Kiik-Koba 1	*H. neanderthalensis*	Male	161.2	Tibia	*150*
Krapina 236	*H. neanderthalensis*	Female	160.0	Lower limb (foot bone)	*148*
Krapina 237	*H. neanderthalensis*	Male	171.1	Lower limb (foot bone)	*148*
Krapina 238.2+238.7	*H. neanderthalensis*	Indet.	164.2	Lower limb (foot bone)	*148*
Krapina 248.1	*H. neanderthalensis*	Indet.	169.9	Lower limb (foot bone)	*148*

Table 14. *Continued.*

Site	Assigned taxon	Sex	Stature (cm)	Element of estimate	Refs
Krapina foot A^2	*H. neanderthalensis*	Female	163.2	Lower limb (foot bone)	*148*
La Chapelle aux Saints	*H. neanderthalensis*	Male	163.6	Humerus	*150*
La Ferrassie 1*	*H. neanderthalensis*	Male	172.9	Ulna	*150*
La Ferrassie 2*	*H. neanderthalensis*	Female	151.3	Upper and lower limb (long bones	*150*
La Quina H1	*H. neanderthalensis*	Indet.	168.8	Foot	*148*
La Quina H5	*H. neanderthalensis*	Female	158.9	Ulna	*148*
Le Ferrassie 2	*H. neanderthalensis*	Female	149.6	Ulna	*148*
Lezetxiki	*H. neanderthalensis*	Male	167.3	Humerus	*148*
Mladec 30	*H. neanderthalensis*	Indet.	173.3	Lower limb (foot bone)	*148*
Moros de la Gabasa	*H. neanderthalensis*	Female	157.9	Lower limb (foot bone)	*148*
Neandertal 1*	*H. neanderthalensis*	Male	165.3	Upper and lower limb (bone)	*148*
Regourdou 1*	*H. neanderthalensis*	Male	162.3	Upper limb bone (long bone)	*150*
SDR-035+SDR-041	*H. neanderthalensis*	Male	160.4	Upper limb	*148*
SDR-054+SDR-055+SDR-056	*H. neanderthalensis*	Male	167.2	Upper limb	*148*
Sedia del Diavolo 2	*H. neanderthalensis*	Female	159.7	Foot	*148*
Shanidar 1*	*H. neanderthalensis*	Male	170.6	Upper limb (long bone)	*150*
Shanidar 2	*H. neanderthalensis*	Male	154.3	Tibia	*148*
Shanidar 4	*H. neanderthalensis*	Male	164.7	Radius	*148*
Shanidar 4	*H. neanderthalensis*	Male	164.4	Ulna	*148*
Shanidar 4	*H. neanderthalensis*	Male	164.6	Upper limb (long bone)	*150*
Shanidar 5*	*H. neanderthalensis*	Indet.	162	Ulna	*150*
Shanidar 6	*H. neanderthalensis*	Female	156.9	Radius	*150*
Shanidar 8	*H. neanderthalensis*	Female	159.3	Lower limb (foot bone)	*148*
Sima de las Palomas 92	*H. neanderthalensis*	Indet.	152.6	Lower limb (long bone)	*148*
Sima de las Palomas 96	*H. neanderthalensis*	Female	149.2	Lower and upper limb (long bone)	*148*
Sindron	*H. neanderthalensis*	Male	167.2	Ulna	*150*
Sindron	*H. neanderthalensis*	Female	159.9	Humerus	*150*
Spy 2*	*H. neanderthalensis*	Male	158.6	Lower limb (long bone)	*150*
Spy 25B	*H. neanderthalensis*	Indet.	161.2	Lower limb (foot bone)	*148*
Spy 25C	*H. neanderthalensis*	Indet.	157.9	Lower limb (foot bone)	*148*
Spy 25D	*H. neanderthalensis*	Indet.	160.3	Lower limb (foot bone)	*148*
Subalyuk 1	*H. neanderthalensis*	Female	160.5	Lower limb (foot bone)	*148*
Tabun 1*	*H. neanderthalensis*	Female	155.7	Lower and upper limb (long bone)	*148*

Table S15. Mass estimates of late Pleistocene *H. sapiens* and *H. neanderthalensis*

Site	**Assigned taxon**	**Sex**	**Mass (kg)**	**Element of estimate**	**Ref**
Abri Pataud 1	*H. sapiens*	Female	69.7	Lower limb (foot bone)	*148*
Baousso de Torre 1	*H. sapiens*	Male	76.9	Femur	*151*
Baousso de Torre 2	*H. sapiens*	Male	72.1	Femur	*151*
Barma Grande 2	*H. sapiens*	Male	79.8	Femur	*151*
Cap Blanc	*H. sapiens*	Female	57.0	Femur	*151*
Caviglione I	*H. sapiens*	Male	65.6	Femur	*151*
Chancellade	*H. sapiens*	Male	66.0	Femur	*151*
Cro-magnon 1 (CM-1)	*H. sapiens*	Male	70.3	femur	*148*
Cro-magnon 4314	*H. sapiens*	Male	70.1	Femur	*148*
Cro-magnon 4315	*H. sapiens*	Male	73.5	Femur	*148*
Cro-magnon 4317	*H. sapiens*	Indet.	61.7	Femur	*148*
Cro-magnon 4321	*H. sapiens*	Indet.	61.3	Femur	*148*
Cro-magnon 4337	*H. sapiens*	Female	81.1	Lower limb (foot bone)	*148*
Dolní Věstonice 13	*H. sapiens*	Male	71.2	Femur	*148*
Dolní Věstonice 14	*H. sapiens*	Male	79.4	Femur	*148*
Dolní Věstonice 15	*H. sapiens*	Male	69.8	Femur	*148*
Dolní Věstonice 16	*H. sapiens*	Male	78.0	Femur	*148*
Dolní Věstonice 3	*H. sapiens*	Female	55.8	Femur	*148*
Fanciulli 4	*H. sapiens*	Male	82.5	Femur	*148*
Fanciulli 5	*H. sapiens*	Female	52.1	Femur	*148*
Gough's Cave 1	*H. sapiens*	Male	70.1	Femur	*148*
Grotte des Enfant 4	*H. sapiens*	Male	82.3	Femur	*151*
Grotte des Enfant 5	*H. sapiens*	Female	60.8	Femur	*151*
Kubbaniya 1	*H. sapiens*	Indet.	71.8	Femur	*148*
La Madelaine	*H. sapiens*	Female	66.0	Femur	*151*
Liujiang 1	*H. sapiens*	Female	42.7	Femur	*148*
Minatogawa 1	*H. sapiens*	Male	63.3	Femur	*148*
Minatogawa 2	*H. sapiens*	Female	48.6	Femur	*148*
Minatogawa 3	*H. sapiens*	Female	50.8	Femur	*148*
Minatogawa 4	*H. sapiens*	Female	47.4	Femur	*148*
Mirón 1	*H. sapiens*	Female	56.9	Femur	*148*
Mittlere Klause 1	*H. sapiens*	Indet.	72.0	Femur	*148*
Mladeč 21	*H. sapiens*	Female	65.6	Femur	*148*
Mladeč 22	*H. sapiens*	Indet.	78.5	Femur	*148*
Mladeč 30	*H. sapiens*	Indet.	91.3	Lower limb (foot bone)	*148*
Obercassel 1	*H. sapiens*	Male	71.0	Femur	*151*
Obercassel 2	*H. sapiens*	Female	53.1	Femur	*151*
Ohalo 2	*H. sapiens*	Male	74.9	Femur	*148*
Omo Kibish 1	*H. sapiens*	Female?	54.1	Lower limb (foot bone)	*148*
Paglicci 25	*H. sapiens*	Female	61.7	Femur	*148*

Table S5. *Continued.*

Site	**Assigned taxon**	**Sex**	**Mass (kg)**	**Element of estimate**	**Ref**
Paviland I	*H. sapiens*	Male	71.5	Femur	*151*
Predmost 14	*H. sapiens*	Female	66.5	Femur	*151*
Predmost 4	*H. sapiens*	Male	68.7	Femur	*151*
Predmost 9	*H. sapiens*	Female	56.3	Femur	*151*
Předmostí 1	*H. sapiens*	Female	56.5	Lower limb (foot bone)	*148*
Předmostí 3	*H. sapiens*	Male	70.1	Femur	*148*
Qafzeh 3	*H. sapiens*	Female	46.7	Lower limb (foot bone)	*148*
Qafzeh 9*	*H. sapiens*	Female	62	Upper and lower limb (long bones)	*148*
Rochette 1	*H. sapiens*	Indet.	66.7	Femur	*148*
Skhul 6	*H. sapiens*	Male	69.0	Femur	*148*
Skhul 9	*H. sapiens*	Male	74.0	Femur	*148*
Skhul IV	*H. sapiens*	Male	72.1	Upper and lower limb (long bones)	*151*
Skhul V	*H. sapiens*	Male	68.1	Humerus	*151*
St Germain la Rive	*H. sapiens*	Female	59.2	Femur	*151*
Sunghir 1	*H. sapiens*	Male	78.9	Femur	*148*
Tagliennte	*H. sapiens*	Male	64.9	Femur	*151*
Tianyuan 1	*H. sapiens*	Indet.	71.4	Lower limb (foot bone)	*148*
Veneri 1	*H. sapiens*	Male	77.1	Femur	*148*
Veneri 2	*H. sapiens*	Female	74.2	Femur	*148*
Zhoukoudian-UC 105	*H. sapiens*	Indet.	71.8	Femur	*148*
Zhoukoudian-UC 117	*H. sapiens*	Indet.	59.0	Femur	*148*
Amud 1	*H. neanderthalensis*	Male	77.9	Femur	*151*
Fond-de-Foret 1	*H. neanderthalensis*	Indet.	73.5	Femur	*148*
Kebara 2	*H. neanderthalensis*	Male	69.3	Femur	*151*
Krapina 207	*H. neanderthalensis*	Male	66.0	Femur	*148*
Krapina 208	*H. neanderthalensis*	Indet.	68.5	Femur	*148*
Krapina 209	*H. neanderthalensis*	Indet.	67.4	Femur	*148*
Krapina 213	*H. neanderthalensis*	Indet.	83.0	Femur	*148*
Krapina 214	*H. neanderthalensis*	Indet.	63.7	Femur	*148*
Krapina 236	*H. neanderthalensis*	Female	59.7	Lower limb (foot bone)	*148*
Krapina 237	*H. neanderthalensis*	Male	77.5	Lower limb (foot bone)	*148*
Krapina 238.1	*H. neanderthalensis*	Indet.	53.0	Lower limb (foot bone)	*148*
Krapina foot A	*H. neanderthalensis*	Female	59.2	Lower limb (foot bone)	*148*
La Chapelle aux Saints	*H. neanderthalensis*	Male	79.8	Femur	*151*
La Ferrassie 1	*H. neanderthalensis*	Male	83.4	Femur	*151*
La Ferrassie 2	*H. neanderthalensis*	Female	65.1	Femur	*151*
La Quina H1	*H. neanderthalensis*	Indet.	72.7	Foot	*148*
Le Ferrassie 2	*H. neanderthalensis*	Female	65.1	Ulna	*151*
Mladec 30	*H. neanderthalensis*	Indet.	91.3	Lower limb (foot bone)	*148*

Table S15. *Continued.*

Site	**Assigned taxon**	**Sex**	**Mass (kg)**	**Element of estimate**	**Ref**
Regourdou 1	*H. neanderthalensis*	Male	65.1	Femur	*151*
SDR-1609	*H. neanderthalensis*	Indet.	82.6	Femur	*148*
Shanidar 4	*H. neanderthalensis*	Male	72.6	Radius	*151*
Shanidar 4	*H. neanderthalensis*	Male	72.6	Ulna	*151*
Shanidar 4	*H. neanderthalensis*	Male	72.6	Femur	*151*
Shanidar 5	*H. neanderthalensis*	Indet.	68.7	Ulna	*151*
Sima de las Palomas 77	*H. neanderthalensis*	Indet.	66.9	Femur	*151*
Sima de las Palomas 92	*H. neanderthalensis*	Indet.	63.7	Femur	*151*
Sima de las Palomas 96	*H. neanderthalensis*	Female	61	Femur	*151*
Sindron	*H. neanderthalensis*	Male	80.1	Ulna	*151*
Spy 2	*H. neanderthalensis*	Male	83.4	Femur	*151*
Tabun 1	*H. neanderthalensis*	Female	62	Femur	*151*

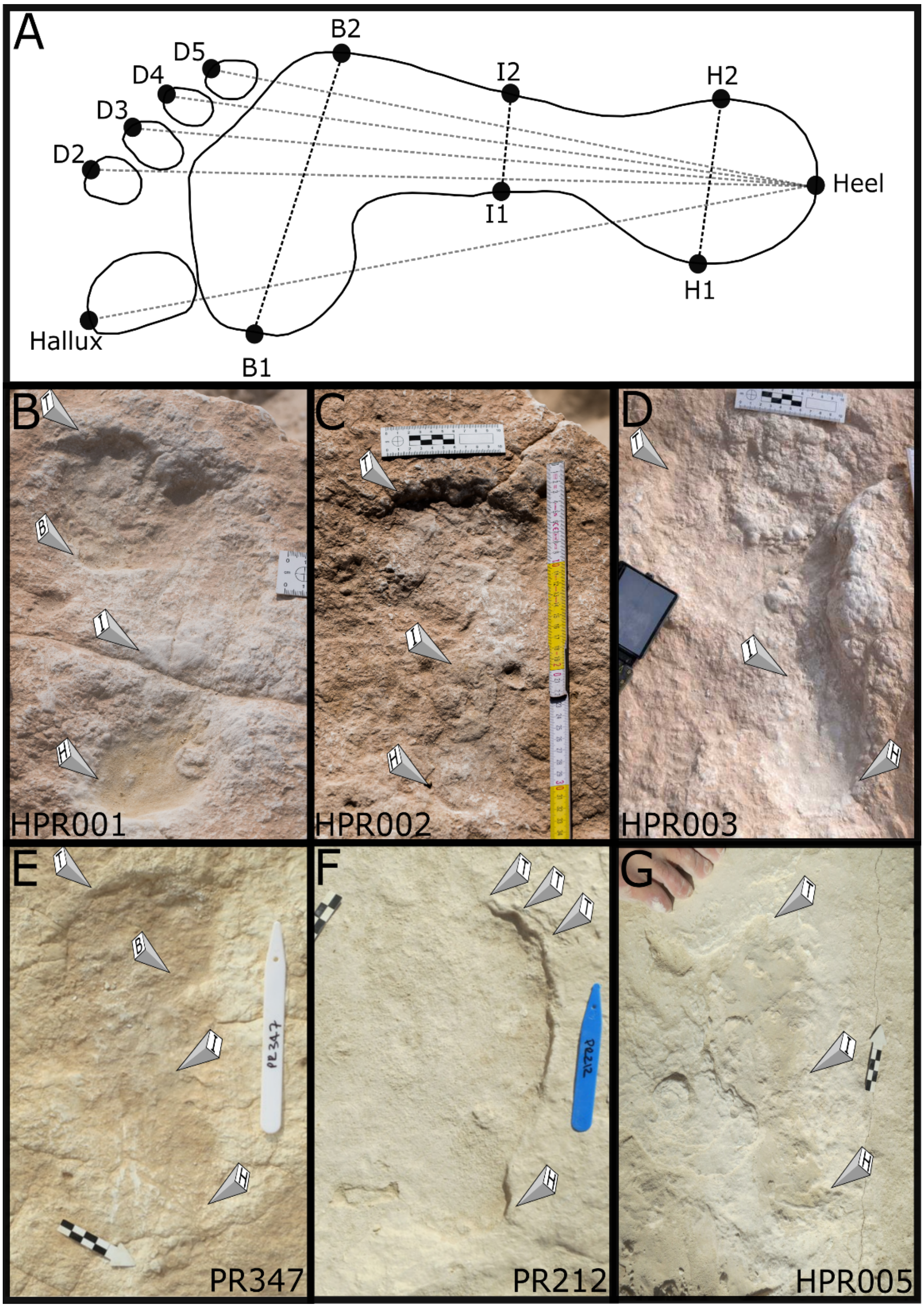

Figure S9. (A) Footprint morphometric data collected in this study (image taken and modified from Ref *111*. **(B-G)** examples of hominin footprints. T, B, H, and I denote toe margin, ball, heel, and instep respectively. Photo credit: Klint Janulis, University of Oxford.

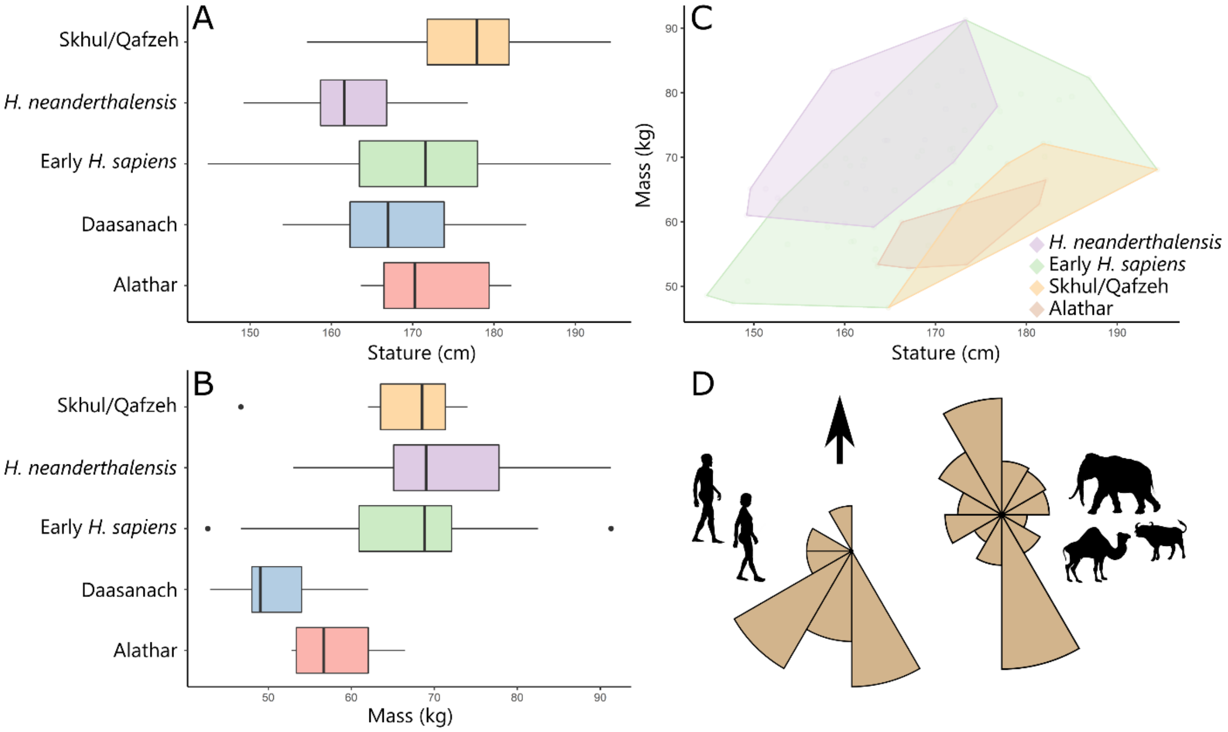

Figure S10. (**A**) Stature estimates (cm) of the Alathar trackmakers compared to present-day humans (Daasanch) and estimates for archaic hominins based on skeletal remains. (**B)** Same as (A) but for body mass (kg). (**C**) Stature and mass scatterplot. (**D**) Roseplots depicting the orientation of hominin and non-hominin mammal tracks. Statute and mass data provided in Tables S14–S15. Data from Ref *59* collected using WebPlotDigitizer (*152*)

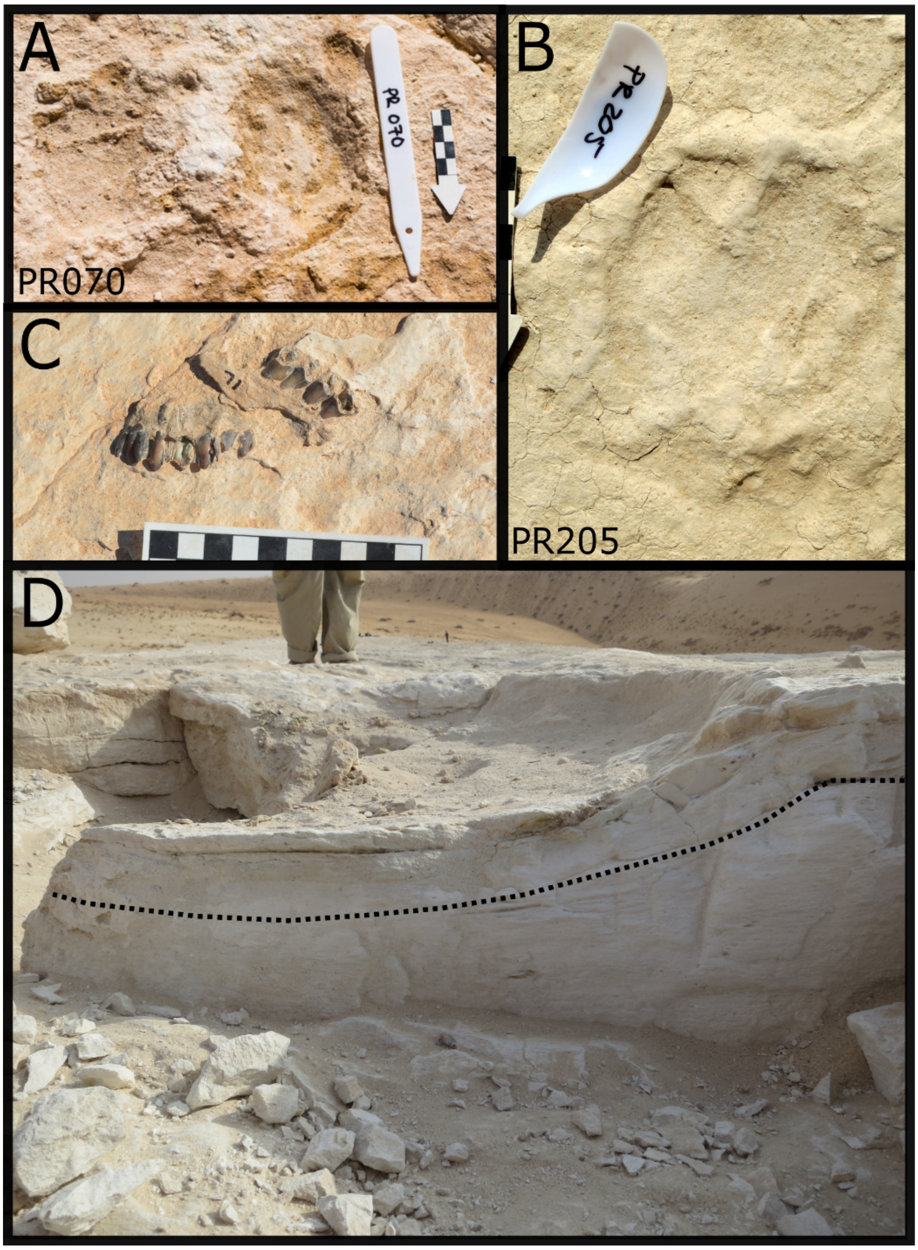

Figure S11. (A) Large buffalo track, *Bijugopeda* isp. **(B)** Medium-sized bovid track, cf. *Pecoripeda* isp. **(C)** Medium-sized bovid maxilla, cf. *Oryx* sp., eroding out of the paleolake surface **(D)** Bisected elephant track exhibiting significant stratigraphic load deformation, as indicated by the black line. Photo credit: Gilbert Price, The University of Queensland.

Supplementary Text 6: Stable isotope analysis of fossil fauna tooth enamel

Background. Recent archaeological (e.g. *15–16, 18*) and fossil (*4*) findings have highlighted the importance of the Arabian Peninsula in the study of hominin prehistory. Climate modelling (*153*), speleothem records (*154–155*), and geomorphological studies of paleolake deposits (*11*) clearly demonstrate that, at times during the Pleistocene, the harsh, hyper-arid deserts spanning Arabia today were replaced by a 'Green Arabia'. This is supported by the fossil record which documents influxes of African, Levantine, and Eurasian fauna into this part of the world during the middle and late Pleistocene (*26, 42, 133*). Nevertheless, there has remained a relative lack of direct insights into how wet 'Green Arabia' was and what this meant for local and regional vegetation and, consequently, animal and hominin adaptations (though see Ref *28*).

Stable carbon isotope ($\delta^{13}C$) analysis of faunal tooth enamel is regularly used to assess different types of biomass in past animal diets (*156–158*), including in the Arabian Peninsula (*28, 133*). Most terrestrial plants, including trees, herbs, shrubs, and shade-loving grasses follow the C_3 photosynthetic pathway (*159*). C_4 photosynthesis is followed by most arid-adapted grasses and some sedges (*160*). C_3 and C_4 plants have distinct and non-overlapping $\delta^{13}C$ values (*161*) that are passed into faunal consumers allowing reliance on tree and shrub versus grassland biomass to be determined in global ecosystems, including those of Arabia (*133*). In faunal diets, prior to the impact of significant fossil fuel emissions, average herbivore $\delta^{13}C$ values for C_3 and C_4 reliance are approximately -12‰ and 0‰, respectively (*156–158*).

The stable oxygen isotope ($\delta^{18}O$) measurement of animal tissues can provide additional paleoecological information about water and food. $\delta^{18}O$ data from fossil herbivore tooth enamel reflect a diversity of parameters including precipitation source, humidity, temperature, and also plant water (*162–164*). Those animals which obtain the majority of their water from plants will strongly reflect those environmental factors that influence plant transpiration and plant $\delta^{18}O$ (*165–167*).

However, multiple potential influences can often make faunal enamel $\delta^{18}O$ difficult to interpret as a paleoenvironmental signal. This is particularly the case in areas like the Arabian Peninsula where the source water, and therefore $\delta^{18}O$, for precipitation may have changed over time (*153*). Evaporation exerts a positive effect on $\delta^{18}O$, particularly in arid desert regions such as the centre of the Arabian Peninsula, so that continental water bodies and soils in areas with a water deficit are ^{18}O-enriched. This effect is even stronger in plants due to the process of evapo-transpiration (*168–169*).

Tooth enamel is primarily made up of a hydroxyapatite crystal lattice that is resistant to post-mortem diagenetic substitution and degradation even across timescales ranging back to the Miocene and beyond (*156, 170–171*). The preserved 'biogenic' structural carbonate provides an accurate signature for the 'bulk diet' of an individual during the period of enamel formation (*156, 172*), unlike bone collagen that is biased towards dietary protein contributions (*172*). Furthermore, since tooth enamel forms incrementally, sequential δ^{13}C and δ^{18}O analysis of animal tooth enamel can be used to look at temporal changes in vegetation and water source during the period of tooth enamel formation (*173).*

Results. Bulk δ^{13}C and δ^{18}O measurements of the fauna analyzed in this study are shown in Table S16 and Figure S12. δ^{13}C results from the Bovidae samples (range = -0.3 to -4.8‰) demonstrate the dominant presence of C_4 biomass in their diets. However, unlike recently published isotope work from fossil fauna at the middle Pleistocene site of Ti's al Ghadah (*c.* 500–300 ka) (*28*) there also appears to be a significant contribution of C_3 vegetation. This could indicate the presence some Bovidae taxa at Alathar with a different feeding focus when compared to the *Oryx* sp. and Hartebeest found at Ti's al Ghadah, a landscape with greater prevalence of C_3 shrubs or sedges, or the existence of some sort of winter rainfall season supporting C_3 grasses. A similar scenario exists for the bulk measurement of the extinct elephant at Alathar (δ^{13}C = -1.8‰) that again shows a strong reliance on C_4 graze but not as strong as seen for *Palaeoloxodon recki* at Ti's al Ghadah (*28*). While CAM plants with δ^{13}C values intermediate between C_3 and C_4 plants could complicate this picture (*174*), they are unlikely to form a significant portion of the diets of the animals analyzed here.

The δ^{18}O values of Bovidae (range = -2.2 to 1.4‰) and elephant analysed at Alathar (-3.6‰) are also lower, and less dispersed, than those seen for bovids, equids, and elephantids at Ti's al Ghadah (*28*). This could indicate more humid conditions at Alathar. However, in the absence of greater taxonomic refinement, notably with regards to identifying obligate and non-obligate drinkers (see Refs *28, 166–167*), this remains speculative. This is particularly the case given that it is known that different precipitation sources in the Indian Ocean, the Mediterranean, and western Africa, with different δ^{18}O values, could all have influenced the groundwater values in the interior of the Arabian Peninsula at different points in the past (*28*, *153*).

The sequential $\delta^{13}C$ data from the elephant analysed here demonstrates a relatively persistent source of vegetation throughout the formation of the tooth, apparently primarily C_4 graze but with some contributions of C_3 grasses, sedges, and/or browse (Table S17; Fig. S13). The sequential $\delta^{18}O$ fails to document any clear seasonal variation in water source or environmental stress, though some fluctuations towards higher values (and potentially higher aridity) are present. Overall, the elephant specimen demonstrates very little variation in either $\delta^{13}C$ or $\delta^{18}O$ suggesting reliable access to stable water bodies and similar types of vegetation on an intra- and inter-annual basis. Such results would in turn imply that, as at Ti's al Ghadah, 'Green Arabia' was not composed of isolated oases, but represented interconnected, regional water sources and vegetation zones that would have been attractive to large-bodied mammals, including hominins moving into and within the Arabian Peninsula (see also Ref *28*).

Table S16. Stable carbon and oxygen isotope values and information relating to the fossil samples analysed in this study. * Denotes specimens also sampled sequentially.

Sample ID	**Tooth sampled**	**Taxa**	**$\delta^{13}C$(‰) (VPDB)**	**S.D.**	**$\delta^{18}O$(‰) (VPDB)**	**S.D.**
WNEF17_1/143	P4	*Oryx* sp.	-4.8	0.1	1.4	0.1
WNEF17_1/111	Indet.	Bovidae	-3.0	0.1	-2.2	0.1
WNEF17_1/214	P4	Bovidae	-2.4	0.1	-0.6	0.1
WNEF17_1/198	M2	*Oryx* sp.	-3.4	0.1	0.0	0.1
WNEF17_1/188	Indet.	Bovidae	-0.8	0.1	0.3	0.1
WNEF17_1/275	Indet.	Bovidae	-1.7	0.1	-0.3	0.1
WNEF17_1/108	Indet.	Bovidae	-0.3	0.1	0.7	0.1
*WNEF17_1/217	Enamel	Elephantidae	-1.8	0.1	-3.6	0.1

Table S17. Sequential $\delta^{13}C$ and $\delta^{18}O$ measurements from fossil Elephantidae (specimen WNEF17_1/217) analysed in this study.

Distance from root-enamel junction	**$\delta^{13}C$ (‰) (VPDB)**	**Standard deviation**	**$\delta^{18}O$ (‰) (VPDB)**	**Standard deviation**
0	0.4	0.1	-1.7	0.1
5	-0.8	0.1	-2.9	0.1
10	-1.1	0.1	-2.9	0.1
15	-0.5	0.1	-0.4	0.1
20	-0.5	0.1	-3.6	0.1
25	-0.7	0.1	-3.5	0.1
30	-0.2	0.1	-2.8	0.1
35	-0.3	0.1	-2.1	0.1
40	-1.2	0.1	-3.0	0.1
45	-1.2	0.1	-3.3	0.1
50	-0.4	0.1	-2.3	0.1
55	-1.2	0.1	-3.8	0.1
60	-0.8	0.1	-3.5	0.1
65	-0.9	0.1	-3.2	0.1
70	-1.5	0.1	-3.1	0.1
75	-1.6	0.1	-3.3	0.1
80	-0.2	0.1	-2.1	0.2
85	-0.8	0.1	-3.2	0.1
90	-0.8	0.1	-3.6	0.1
95	-0.8	0.1	-3.3	0.1
100	-2.3	0.1	-4.0	0.1
105	-1.8	0.1	-3.4	0.1
110	0.3	0.1	-1.8	0.1
115	-0.7	0.1	-2.9	0.1
BULK	-1.8	0.1	-3.6	0.1

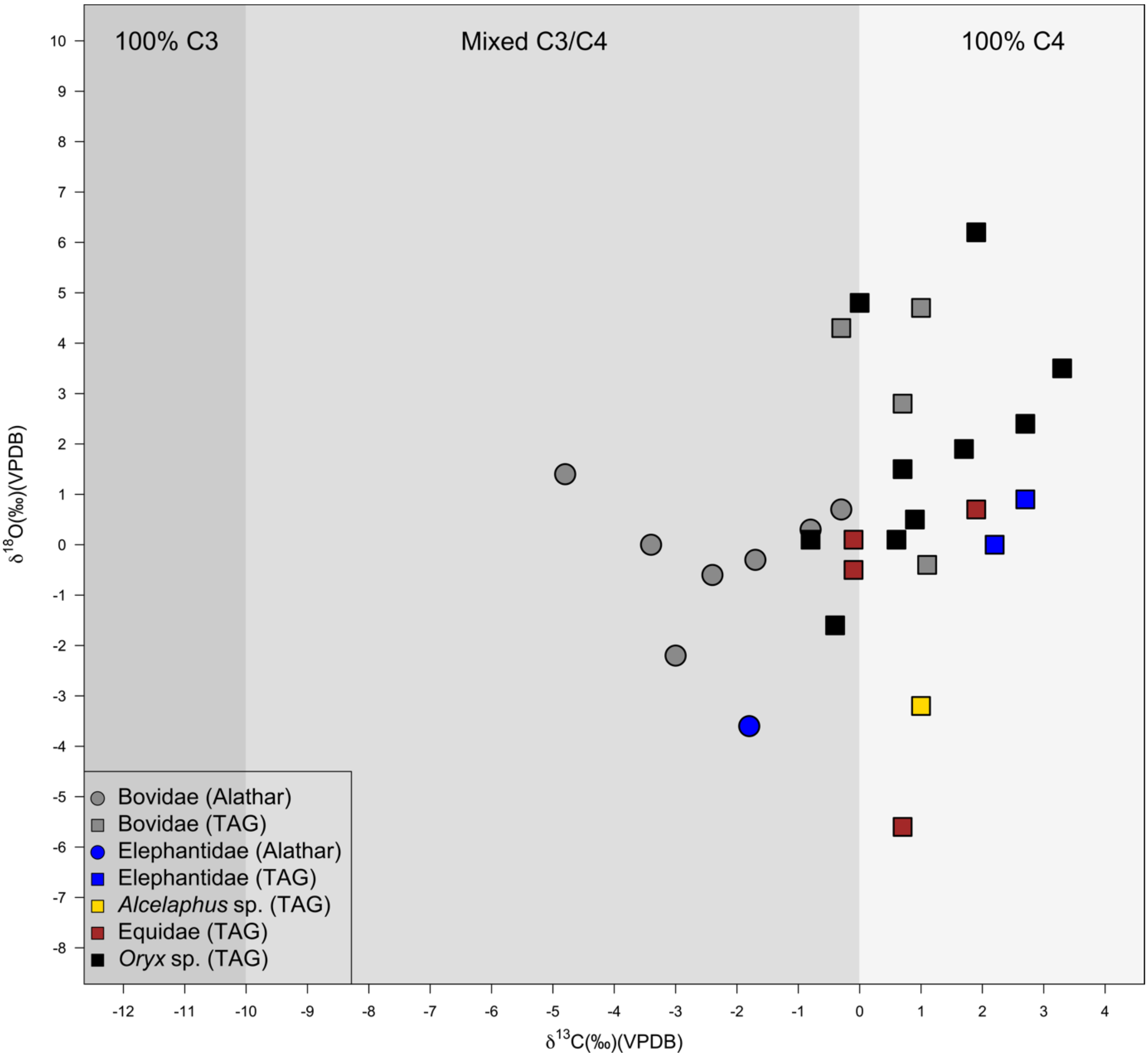

Figure S12. Stable carbon ($\delta^{13}C$) and oxygen ($\delta^{18}O$) isotope values and information relating to the fossil samples analysed in this study and those from Ti's al Ghadah (*28*).

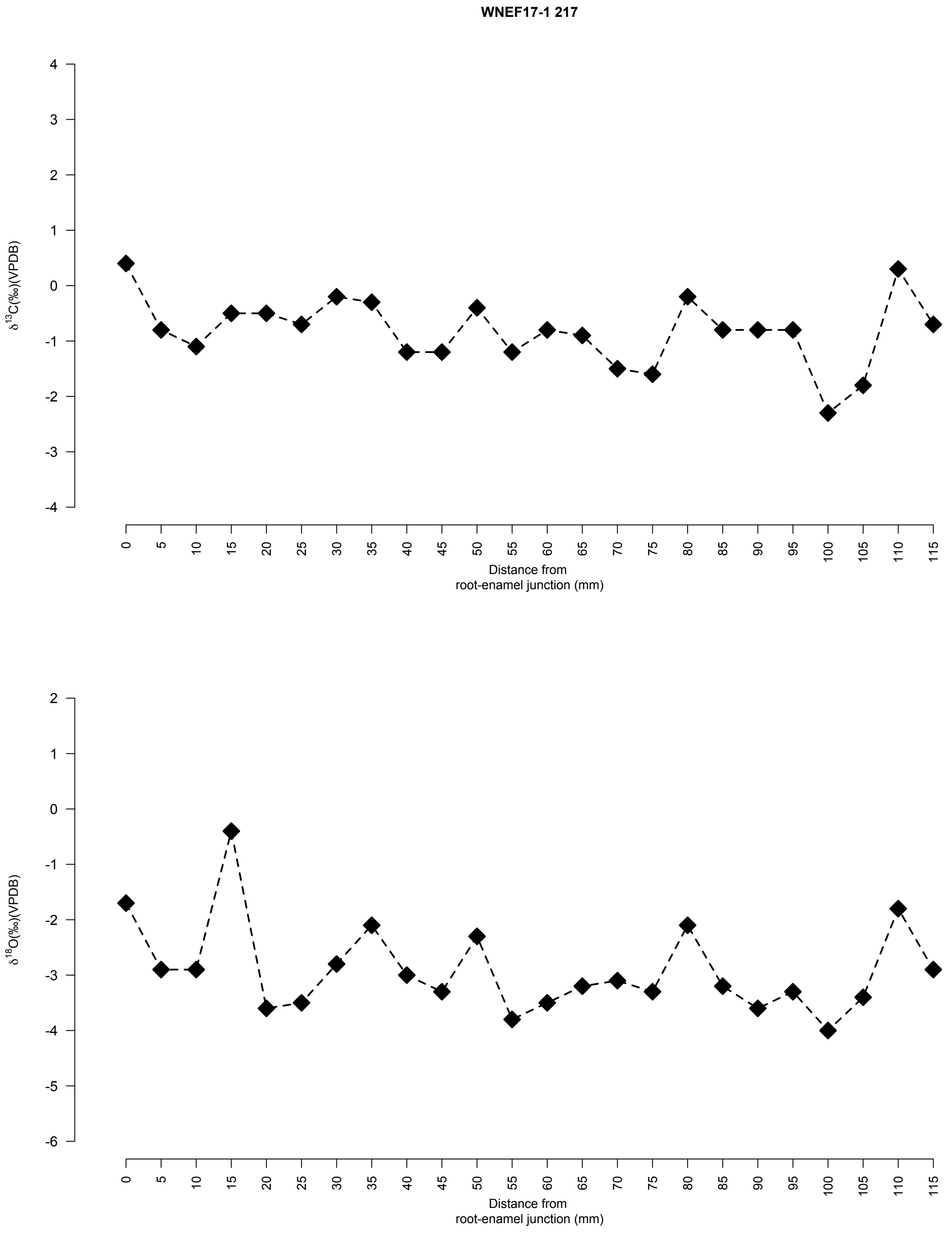

Figure S13. Sequential $\delta^{13}C$ and $\delta^{18}O$ measurements from fossil Elephantidae (specimens WNEF17_1/217) analysed in this study.

REFERENCES AND NOTES

1. H. J. O’Regan, A. Turner, L. C. Bishop, S. Elton, A. L. Lambm, Hominins without fellow travellers? First appearances and inferred dispersals of Afro-Eurasian large-mammals in the Plio-Pleistocene. *Quat. Sci. Rev.* **30**, 1343–1352 (2011).

2. K. Harvati, C. Röding, A. M. Bosman, F. A. Karakostis, R. Grün, C. Stringer, P. Karkanas, N. C. Thompson, V. Koutoulidis, L. A. Moulopouls, V. G. Gorgoulis, M. Kouloukoussa, Apidima Cave fossils provide earliest evidence of *Homo sapiens* in Eurasia. *Nature* **571**, 500–504 (2019).

3. I. Hershkovitz, G. W. Weber, R. Quam, M. Duval, R. Grün, L. Kinsley, A. Ayalon, M. Bar-Matthews, H. Valladas, N. Mercier, J. L. Arsuaga, M. Martinón-Torres, J. M. Bermúdez de Castro, C. Fornai, L. Martín-Francés, R. Sarig, H. May, V. A. Krenn, V. Slon, L. Rodríguez, R. García, C. Lorenzo, J. M. Carretero, A. Frumkin, R. Shahack-Gross, D. E. B.-Y. Mayer, Y. Cui, X. Wu, N. Peled, I. Groman-Yaroslavski, L. Weissbrod, R. Yeshurun, A. Tsatskin, Y. Zaidner, M. Weintein-Evron, The earliest modern humans outside Africa. *Science* **359**, 456–459 (2018).

4. H. S. Groucutt, R. Grün, I. S. Zalmout, N. A. Drake, S. J. Armitage, I. Candy, R. Clark-Wilson, J. Louys, P. S. Breeze, M. Duval, L. T. Buck, T. L. Kivell, E. Pomeroy, N. B. Stephens, J. T. Stock, M. Stewart, G. J. Price, L. Kinsley, W. W. Sung, A. Alsharekh, A. al-Omari, M. Zahir, A. M. Memesh, A. J. Abdulshakoor, A. M. Al-Masari, A. A. Bahameen, K. M. S. Al Murayyi, B. Zahrani, E. M. L. Scerri, M. D. Petraglia, *Homo sapiens* in Arabia by 85,000 years ago. *Nat. Ecol. Evol.* **2**, 800–809 (2018).

5. P. Roberts, B. A. Stewart, Defining the ‘generalist specialist’ niche for Pleistocene *Homo sapiens*. *Nat. Hum. Behav.* **2**, 542–550 (2018).

6. R. Grün. C. Stringer, F. McDermott, R. Nathan, N. Porat, S. Robertson, L. Taylor, G. Mortimer, S. Eggins, M. McCulloch, U-series and ESR analyses of bones and teeth relating to the human burials from Skhul. *J. Hum. Evol.* **49**, 316–334 (2005).

7. N. T. Roach, K. G. Hatala, K. R. Ostrofsky, B. Villmoare, J. S. Reeves, A. Du, D. R. Braun, J. W. K. Harris, A. K. Behrensmeyer, B. G. Richmond, Pleistocene footprints show intensive use of lake margin habitats by *Homo erectus* groups. *Sci. Rep.* **6**, 26374 (2016).

8. K. Hatala, N. T. Roach, K. R. Ostrofsky, R. E. Wunderlich, H. L. Dingwall, B. A. Villmoare, D. J. Green, J. W. K. Harris, D. R. Braun, B. G. Richmond, Footprints reveal direct evidence of group behaviour and locomotion in *Homo erectus*. *Sci. Rep.* **6**, 28766 (2016).

9. A. Cohen, M. Lockley, J. Halfpenny, A. E. Michel, Modern vertebrate track taphonomy at Lake Manyara, Tanzania. *Palaois* **6**, 371–389 (1991).

10. A. Parton, L. Clark-Balzan, A. G. Parker, G. W. Preston, W. W. Sung, P. S. Breeze, M. J. Leng, H. S. Groucutt, T. S. White, A. Alsharekh, M. D. Petraglia, Middle-late Quaternary palaeoclimate variability from lake and wetland deposits in the Nefud Desert, northern Arabia. *Quat. Sci. Rev.* **202**, 78–97 (2018).

11. T. M. Rosenberg, F. Preusser, J. Risberg, A. Plikk, K. A. Kadi, A. Matter, D. Fleitmann, Middle and late Pleistocene humid periods recorded in palaeolake deposits of the Nafud desert, Saudi Arabia. *Quat. Sci. Rev.* **70**, 109–123 (2013).

12. P. S. Breeze, H. S. Grocutt, N. A. Drake, T. S. White, R. P. Jennings, M. D. Petraglia, Palaeohydrological corridors for hominin dispersals in the Middle East ~250–70,000 years ago. *Quat. Sci. Rev.* **144**, 155–185 (2016).

13. I. Thrash, G. K. Theron, J. P. Bothma, Dry season herbivore densities around drinking troughs in the Kruger National Park. *J. Arid Environ.* **29**, 213–219 (1995).

14. M. Valeix, A. J. Loveridge, Z. Davidson, H. Madzikanda, H. Fritz, D. W. Macdonald, How key habitat features influence large terrestrial carnivore movements: Waterholes and African lions in a semi-arid savanna of north-western Zimbabwe. *Landsc. Ecol.* **25**, 337–351 (2010).

15. S. J. Armitage, S. A. Jasim, A. E. Marks, A. G. Parker, V. I. Usik, H.-P. Uerpmann, The southern route “out of Africa”: Evidence for an early expansion of modern humans into Arabia. *Science* **331**, 453–456 (2011).

16. M. D. Petraglia, A. Alsharekh, P. S. Breeze, C. Clarkson, R. Crassard, N. A. Drake, H. S. Groucutt, R. Jennings, A. G. Parker, A. Parton, R. G. Roberts, C. Shipton, C. Matheson, A. al-Omari, M.-A. Veall, Hominin dispersal into the Nefud Desert and Middle Palaeolithic settlement along the Jubbah Palaeolake, northern Arabia. *PLOS ONE* **7**, e49840 (2012).

17. R. Crassard, Y. H. Hilbert, A Nubian complex site from central Arabia: Implications for Levallois taxonomy and human dispersals during the upper Pleistocene. *PLOS ONE* **8**, e69221 (2013).

18. H. S. Groucutt, T. S. White, L. Clark-Balzan, A. Parton, R. Crassard, C. Shipton, R. P. Jennings, A. G. Parker, P. S. Breeze, E. M. L. Scerri, A. Alsharekh, M. D. Petraglia, Human occupation of the Arabian Empty Quarter during MIS 5: Evidence from Mundafan Al-Buhayrah, Saudi Arabia. *Quat. Sci. Rev.* **119**, 116–135 (2015).

19. E. M. L. Scerri, P. S. Breeze, A. Parton, H. S. Groucutt, T. S. White, C. Stimpson, L. Clark-Balzan, R. Jennings, A. Alsharekh, M. D. Petraglia, Middle and late Pleistocene human habitation in the western Nefud, Saudi Arabia. *Quat. Int.* **382**, 200–214 (2015).

20. J. J. Shea. Transition or turnovers? Climatically-forced extinctions of Homo sapiens and Neanderthals in the east Mediterranean Levant. *Quat. Sci. Rev.* **27**, 2253–2270 (2008).

21. P. S. Breeze, H. S. Groucutt, N. A. Drake, J. Louys, E. M. L. Scerri, S. J. Armitage, I. S. A. Zalmout, A. M. Memesh, M. A. Haptari, S. A. Soubhi, A. H. Matari, M. Zahir, A. al-Omari, A. Alsharekh, M. D. Petraglia, Prehistory and palaeoenvironments of the western Nefud Desert, Saudi Arabia. *Arch. Res. Asia* **10**, 1–16 (2017).

22. C. R. Thouless, Long distance movements of elephants in northern Kenya. *Afr. J. Ecol.* **33**, 321–334 (1995).

23. R. M. Laws, I. S. C. Parker, R. C. B. Johnstone, *The Ecology of Elephants in North Bunyoro, Uganda* (Clarendon Press, 1975).

24. M. Ben-Dor, A. Gopher, I. Hershkovitz, R. Barkai, Man the fat hunter: The demise of *Homo erectus* and the emergence of a new hominin lineage in the middle Pleistocene (ca. 400 kyr) Levant. *PLOS ONE* **6**, e28689 (2011).

25. M. Stewart, J. L. Louys, P. S. Breeze, R. Clark-Wilson, N. A. Drake, E. M. L. Scerri, I. S. Zalmout, Y. S. A. Al-Mufarreh, S. A. Soubhi, M. A. Haptari, A. M. Alsharekh, H. S. Groucutt, M. D. Petraglia, A taxonomic and taphonomic study of Pleistocene fossil deposits from the western Nefud Desert, Saudi Arabia. *Quat. Res.* **95**, 1–22 (2020).

26. M. Stewart, J. Louys, G. J. Price, N. A. Drake, H. S. Groucutt, M. D. Petraglia, Middle and late Pleistocene mammal fossils of Arabia and surrounding regions: Implications for biogeography and hominin dispersals. *Quat. Int.* **515**, 12–29 (2019).

27. G. Haynes, On watering holes, mineral licks, death, and predation, in *Environments and Extinctions: Man in Late Glacial North America*, J. Mead, D. Meltzer, Eds. (Centre for the Study of Early Man, 1985), pp. 53–71.

28. P. Roberts, M. Stewart, A. N. Alagaili, P. S. Breeze, I. Candy, N. Drake, H. S. Groucutt, E. M. L. Scerri, J. Lee-Thorp, J. Louys, I. S. Zalmout, Y. S. A. Al-Mufarreh, J. Zech, A. Alsharekh, A. al-Omari, N. Boivin, M. D. Petraglia, Fossil herbivore stable isotopes reveal middle Pleistocene hominin palaeoenvironment in 'Green Arabia'. *Nat. Ecol. Evol.* **2**, 1871–1878 (2018).

29. G. P. Nicholas, Prehistoric hunter-gatherers in wetland environments: Theoretical issues, economic organization and resource management strategies, in *Wetland Archaeology and Environments: Regional Issues, Global Perspectives*, M. C. Lillie, S. Ellis, Eds. (Oxbow Books, 2007), pp. 46–62.

30. N. Boivin, D. Q. Fuller, R. Dennell, R. Allaby, M. D. Petraglia, Human dispersal across diverse environments of Asia during the Upper Pleistocene. *Quat. Int.* **300**, 32–47 (2013).

31. S. J. Gale, P. G. Hoare, *Quaternary Sediments: Petrographic Methods for the Study of Unlithified Rocks* (Belhaven and Halsted Press, 1991).

32. A. P. Palmer, J. A. Lee, R. A. Kemp, S. J. Carr, *Revised Laboratory Procedures for the Preparation of Thin Sections from Unconsolidated Sediments* (Centre for Micromorphology Publication, 2008).

33. S. Juggins, C2 versions 1.7.7. User guide. Software for ecological and palaeoecological data analysis and visualization (Newcastle University, 2016), p. 73.

34. R. W. Battarbee, S. Juggins, F. Gasse, N. J. Anderson, H. Bennion, N. G. Cameron, D. B. Ryves, C. Pailles, F. Chalie, R. Telford, “The European Diatom Database (EDDI): An information system for palaeoenvironmental reconstruction” (Environmental Change Research Centre Research Report No. 81, Department of Geography, University College London, 2001), p. 94.

35. F. Gasse, S. Juggins, L. B. Khelifa, Diatom-based transfer functions for inferring past hydrochemical characteristics of African lakes. *Palaeogeogr. Palaeoclimatol. Palaeoecol.* **177**, 31–54 (1995).

36. L. Bøtter-Jensen, C. E. Andersen, G. A. Duller, A. S. Murray, Developments in radiation, stimulation and observation facilities in luminescence measurements. *Radiat. Meas.* **37**, 535–541 (2003).

37. A. S. Murray, A. G. Wintle, Luminescence dating of quartz using an improved single-aliquot regenerative-dose protocol. *Radiat. Meas.* **32**, 57–73 (2000).

38. R. F. Galbraith, R. G. Roberts, J. M. Olley, H. Yoshida, G. M. Laslett, Optical dating of single and multiple grains of quartz from Jinmium Rock Shelter, Northern Australia: Part I, experimental design and statistical models, *Archaeometry* **41**, 339–364 (1999).

39. L. Bøtter-Jensen, V. Mejdahl, Assessment of beta dose-rate using a GM multicounter system. *Int. J. Radiat. Appl. Instrum. D* **14**, 187–191 (1988).

40. F. De Corte, D. Vandenberghe, S. Hossain, A. De Wispelaere, J. P. Buylaert, P. Van den Haute, Preparation and characterization of loess sediment for use as a reference material in the annual radiation dose determination for luminescence dating. *J. Radioanal. Nucl. Chem.* **272**, 311–319 (2007).

41. J. R. Prescott, J. T. Hutton, Cosmic ray and gamma ray dosimetry for TL and ESR. *Int. J. Radiat. Appl. Instrum. D* **14**, 223–227 (1988).

42. C. M. Stimpson, A. Lister, A. Parton, L. Clark-Balzan, P. S. Breeze, N. A. Drake, H. S. Groucutt, R. Jennings, E. M. L. Scerri, T. S. White, M. Zhair, M. Duval, R. Grün, A. Al-Omari, K. S. M. Al Murayyi, I. S. Zalmout, Y. A. Mufarreh, A. M. Memesh, M. D. Petraglia, Middle Pleistocene vertebrate fossils from the Nefud Desert, Saudi Arabia. *Quat. Sci. Rev.* **143**, 13–36 (2016).

43. R. Grün, Methods of dose determination using ESR spectra age estimates on tooth enamel. *Quat. Geochronol.* **4**, 231–232 (2000)

44. R. Grün, S. Brumby, The assessment of errors in past radiation doses extrapolated from ESR/TL dose-response data. *Radiat. Meas.* **23**, 307–315 (1994).

45. T. R. Clark, G. Roff, J.-x. Zhao, Y.-x. Feng, T. J. Done, J. M. Pandolfi, Testing the precision and accuracy of the U-Th chronometer for dating coral mortality events in the last 100 years. *Quat. Geochronol.* **23**, 35–45 (2014).

46. J.-x. Zhao, K.-f. Yu, Y.-x. Feng, High-precision 238U-234U-230$^{\mathrm{Th}}$ disequilibrium dating of the recent past: A review. *Quat. Geochronol.* **4**, 423–433 (2009).

47. R. Grün. O. Katzenberger, An alpha irradiator for ESR dating. *Ancient TL* **12**, 35–38 (1994).

48. R. E. Marsh, "Beta-gradient isochrones using electron paramagnetic resonance: Towards a new dating method in archaeology," thesis, McMaster University, Hamilton, Ontario (1999).

49. G. Guérin, N. Mercier, G. Adamiec, Dose-rate conversion factors: Update. *Ancient TL* **29**, 5–8 (2011).

50. J. R. Prescott, J. T. Hutton, Cosmic ray contributions to dose rates for luminescence and ESR dating: Large depths and long-term time variations. *Radiat. Meas.* **23**, 497–500 (1994).

51. Q. Shao, J.-J. Bahain, J.-M. Dolo, C. Falguères, Monte Carlo approach to calculate US-ESR age and age uncertainty for tooth enamel. *Quat. Geochronol.* **22**, 99–106 (2014).

52. R. Grün, H. P. Schwarcz, J. Chadam, ESR dating of tooth enamel: Coupled correction for U-uptake and U-series disequilibrium. *Int. J. Rad. Appl. Instrum. D* **14**, 237–241 (1988).

53. Q. Shao, J.-J. Bahain, C. Falguères, J.-M. Dolo, T. Garcia, A new U-uptake model for combined ESR/U-series dating of tooth enamel. *Quat. Geochronol.* **10**, 406–411 (2012).

54. R. Grün, The DATA program for the calculation of ESR age estimates on tooth enamel. *Quat. Geochronol.* **4**, 231–232 (2009).

55. R. Grün, An alternative model for open system U-series/ESR age calculations: (Closed-system U-series)-ESR, CSUS-ESR. *Ancient TL* **18**, 1–4 (2000).

56. A. K. Behrensmeyer, Taphonomic and ecological information from bone weathering. *Paleobiology* **4**, 150–162 (1978).

57. H. T, Bunn, "Meat-eating and human evolution: Studies on the diet and subsistence patterns of Plio-Pleistocene hominids in East Africa," thesis, University of Wisconsin, Madison (1982).

58. M. R. Bennett, S. A. Morse, *Human Footprints: Fossilised Locomotion* (Springer, 2014).

59. H. L. Dingwall, K. G. Hatala, R. E. Wunderlich, B. G. Richmond, Hominin stature, body mass, and walking speed estimates based on 1.5 million-year-old fossil footprints at Ileret. *J. Hum. Evol.* **64**, 556–568 (2013).

60. M. Sponheimer, J. A. Lee-Thorp, D. de Ruiter, D. Codron, J. Codron, A. T. Baugh, F. Thackeray, Hominins, sedges, and termites: New carbon isotope data from Sterkfontein Valley and Kruger National Park. *J. Hum. Evol.* **48**, 301–312 (2005).

61. J. A. Lee-Thorp, A. Likius, H. T. Mackaya, P. Vignaud, M. Sponheimer, M. Brunet, Isotopic evidence for an early shit to C_4 resources by Pliocene hominins in Chad. *Proc. Natl. Acad. Sci. U.S.A.* **11**, 20369–20372 (2012).

62. L. E. Lisiecki, M. E. Raymo, A Plio-Pleistocene stack of 57 globally distributed benthic $\delta^{18}0$ records. *Paleoceanography* **20**, PA1003 (2005).

63. N. Mercier, H. Valladas, O. Bar-Yosef, B. Vandermeersch, C. Stringer, J.-L. Joron, Thermoluminescence date for the Mousterian burial site of Es-Skhul, Mt. Carmel. *J. Arch. Sci.* **20**, 167–174 (1993).

64. H. Valladas, J. L. Reyss, J. L. Joron, G. Valladas, O. Bar-Yosef, B. Vandermeersch, Thermoluminescence dating of Mousterian Troto-Cro-Magnon' remains from Israel and the origin of modern man. *Nature* **331**, 614–616 (1988).

65. H. S. Groucutt, E. M. L. Scerri, C. Stringer, M. D. Petraglia, Skhul lithic technology and the dispersal of *Homo sapiens* into southwest Asia. *Quat. Int.* **515**, 30–52 (2019).

66. A. Berger, M. F. Loutre, Insolation values for the climate of the last 10 million years. *Quat. Sci. Rev.* **10**, 297–317 (1991).

67. V. J. Jones, S. Juggins, The construction of a diatom-based chlorophyll *a* transfer function and its application at three lakes on Signy Island (Maritime Antarctic) subject to differing degrees of nutrient enrichment. *Freshw. Biol.* **34**, 433–445 (1995).

68. D. B. Ryves, S. Juggins, S. C. Fritz, R. W. Battarbee, Experimental diatom dissolution and the quantification of microfossil preservation in sediments. *Palaeogeogr. Palaeoclimatol. Palaeoecol.* **172**, 99–113 (2001).

69. D. B. Ryves, R. W. Battarbee, S. Juggins, S. C. Fritz, N. J. Anderson, Physical and chemical predictors of diatom dissolution in freshwater and saline lake sediments in North America and West Greenland. *Limnol. Oceanogr.* **51**, 1355–1368 (2006).

70. K. L. Loakes, D. B. Ryves, H. F. Lamb, F. Schäbitz, M. Dee, J. J. Tyler, K. Mills, S. McGowan, Late quaternary climate change in the north-eastern highlands of Ethiopia: A high resolution 15,600 year diatom and pigment record from Lake Hayk. *Quat. Sci. Rev.* **202**, 166–181 (2018).

71. R. J. Flower, Diatom preservation: Experiments and observations on dissolution and breakage in modern and fossil material. *Hydrobiologia* **269–270**, 473–484 (1993).

72. J. M. Reed, Diatom preservation in the recent sediment record of Spanish saline lakes: Implications for palaeoclimate study. *J. Paleolimnol.* **19**, 129–137 (1998).

73. J. D. Collinson, Alluvial sediments, in *Sedimentary Environments: Processes, Facies and Stratigraphy*, H. G. Reading, Ed. (Blackwell, 1996), pp. 37–81.

74. M. R. Talbot, P. A. Allen, Lakes, in *Sedimentary Environments: Processes, Facies and Stratigraphy*, H. G. Reading, Ed. (Blackwell, 1996), pp. 83–123.

75. S. J. Armitage, R. M. Bailey, The measured dependence of laboratory beta dose rates on sample grain size. *Radiat. Meas.* **39**, 123–127 (2005).

76. R. G. Roberts, R. F. Galbraith, J. M. Olley, H. Yosida, G. M. Laslett, Optical dating of single and multiple grains of quartz from Jinmium rock shelter, northern Australia: Part II, results and implications. *Archaeometry* **41**, 365–395 (1999).

77. G. A. T. Duller, Assessing the error on equivalent dose estimates derived from single aliquot regenerative dose measurements. *Ancient TL* **25**, 15–24 (2007).

78. C. Burow, calc_AliquotSize(): Estimate the amount of grains on an aliquot. Function version 1.3.2, in S. Kreutzer, M. Dietze, C. Burrow, M. C. Fuchs, C. Schmidt, M. Fischer, J. Friedrich, *Luminescence: Comprehensive Luminescence Dating Data Analysis. Rpackage Version 0.7.5* (2017); https://CRAN.R-project.org/package=Luminescence.

79. G. A. T. Duller, Distinguishing quartz and feldspar in single grain luminescence measurements. *Radiat. Meas.* **37**, 161–165 (2003).

80. A. G. Wintle, A. S. Murray, A review of quartz optically stimulated luminescence characteristics and their relevance in single-aliquot regeneration dating protocols. *Radiat. Meas.* **41**, 369–391 (2006).

81. A. G. Wintle, G. Adamiec, Optically stimulated luminescence signals from quartz: A review. *Radiat. Meas.* **98**, 10–33 (2017).

82. C. Burow, calc_CentralDose(): Apply the central age model (CAM) after Galbraith et al. (1999) to a given De distribution. Function version 1.3.2, in S. Kreutzer, M. Dietze, C. Burrow, M. C. Fuchs, C. Schmidt, M. Fischer, J. Friedrich, *Luminescence: Comprehensive Luminescence Dating Data Analysis. Rpackage Version 0.7.5* (2017); https://CRAN.R-project.org/package=Luminescence.

83. S. J. Armitage, A. Krishna, L. E. Parker, G. E. King, Optically stimulated luminescence dating of heat retainer hearths from the Sahara: Insights into signal accumulation and measurement. *Quat. Geochronol.* **45**, 249–253 (2019).

84. Y. S. Mayya, P. Morthekai, M. K. Murari, A. K Singhvi, Towards quantifying beta microdosimetric effects in single-grain quartz dose distribution. *Radiat. Meas.* **41**, 1032–1039 (2006).

85. G. Guérin, A. S. Murray, M Jain, K. J. Thomsen, N. Mercier, How confident are we in the chronology of the transition between Howieson's Poort and Still Bay? *J. Hum. Evol.* **64**, 314–317 (2013).

86. V. Mejdahl, Thermoluminescence dating: beta-dose attenuation in quartz grains. *Archaeometry* **21**, 61–72 (1979).

87. W. T. Bell, Attenuation factors for the absorbed radiation dose in quartz inclusions for thermoluminescence dating. *Ancient TL* **8**, 12 (1979).

88. G. A. T. Duller, The age of the Koputaroa dunes, southwest North Island, New Zealand. *Palaeogeogr. Palaeoclimatol. Palaeoecol.* **121**, 105–114 (1996).

89. J. A. Durcan, G. E. King, G. A. T. Duller, DRAC: Dose Rate and Age Calculator for trapped charge dating. *Quat. Geochronol.* **28**, 54–61 (2015).

90. M. Dietze, S. Kreutzer. Plot_AbanicoPlot(): Function to create an Abanico Plot. Function version 1.3.2, in S. Kreutzer, M. Dietze, C. Burrow, M. C. Fuchs, C. Schmidt, M. Fischer, J. Friedrich,

Luminescence: Comprehensive Luminescence Dating Data Analysis. Rpackage Version 0.7.5 (2017); https://CRAN.R-project.org/package=Luminescence.

91. M. Dietze, S. Kreutzer, C. Burow, M. C. Fuchs, M. Fischer, C. Schmidt, The abanico plot: Visualising chronometric data with individual standard errors. *Quat. Geochronol.* **31**, 12–18 (2016).

92. M. Duval, R. Grün, Are published ESR dose assessments on fossil tooth enamel reliable? *Quat. Geochronol.* **31**, 19–27 (2016).

93. A. W. G. Pike, R. E. M. Hedges, Sample geometry and U uptake in archaeological teeth: Implication for U-series and ESR dating. *Quat. Sci. Rev.* **20**, 2012–2025 (2001).

94. M. Sambridge, R. Grün, S. Eggins, U-series dating of bone in an open system: The diffusion-adsorption-decay model. *Quat. Geochronol.* **9**, 42–53 (2012).

95. M. Duval, C. Falguères, J. -J. Bahain, Age of the oldest hominin settlements in Spain: Contribution to the combined U-series/ESR dating method applied to fossil teeth. *Quat. Geocrhonol.* **10**, 412–417 (2012).

96. J.-J. Bahain, Y. Yokoyama, C. Falguères, M. N. Sarcia, ESR dating of tooth enamel: A comparison with K-Ar dating. *Quat. Sci. Rev.* **11**, 245–250 (1992).

97. W. J. Rink, H. P. Schwarcz, H. K. Lee, J. Rees-Jones, R. Rabinovich, E. Hovers, Electron spin resonance (ESR) and thermal ionization mass spectrometric (TIMS) 230Th/234U dating of teeth in Middle Paleolithic layers at Amud Cave, Israel. *Geoarchaeology* **16**, 701–717 (2001).

98. M. Duval, L. Martin, An application of DosiVox to ESR dating of fossil teeth: Evaluating the impact of dental tissue thickness on the external beta dose rate evaluation. *Geochronometria* **46**, 102–110 (2019).

99. H. Cheng, R. L. Edwards, J. Hoff, C. D. Gallup, D. A. Richards, Y. Asmerom, The half-lives of uranium-234 and thorium-230. *Chem. Geol.* **169**, 17–33 (2000).

100. M. Stewart, J. Louys, H. S. Groucutt, I. Candy, R. Clark-Wilson, P. S. Breeze, N. A. Drake, G. J. Price, Y. S. A. Al-Mufarreh, S. A. Soubhi, I. S. Zalmout, A. M. Alsharekh, A. al-Omari, M. D. Petraglia, Taphonomic and zooarchaeological investigations at the middle Pleistocene site of Ti's al Ghadah, western Nefud Desert, Saudi Arabia. *Quat. Sci. Rev.* **218**, 228–253 (2019).

101. H. A. McClure, “Late Quaternary palaeoenvironments of the Rub’ al Khali”, thesis, University College, London (1984).

102. N. Ashton, S. G. Lewis, I. De Groote, S. M. Duffy, M. Bates, R. Bates, P. Hoare, M. Lewis, S. A. Parfitt, S. Peglar, C. Williams, C. Stringer, Hominin footprints from early Pleistocene deposits at Happisburgh, UK. *PLOS ONE* **9**, e88329 (2014).

103. A. L. A. Wiseman, I. De Groote, A three-dimensional geometric morphometric study of the effects of erosion on the morphologies of modern and prehistoric footprints. *J. Archaeol. Sci. Rep.* **17**, 93–102 (2018).

104. B. Zimmer, G. Pierce-Liutkus, S. T. Marshall, K. G. Hatala, A. Metallo, V. Rossi, Using differential structure-from-motion photogrammetry to quantify erosion at the Engare Sero footprint site, Tanzania. *Quat. Sci. Rev.* **198**, 226–241 (2018).

105. J. Duveau, G. Berillon, C. Verna, G. Laisne, D. Cliquet, The composition of a Neanderthal social group revealed by the hominin footprints at Le Rozel (Normandy, France). *Proc. Natl. Acad. Sci. U.S.A.* **116**, 19409–19414 (2019).

106. M. D. Leakey, R. L. Hay, Pliocene footprints in the Laetoli Beds at Laetoli, northern Tanzania. *Nature* **278**, 317–323 (1979).

107. M. H. Day, E. H. Wickens, Laetoli Pliocene hominid footprints and bipedalism. *Nature* **286**, 385–387 (1980).

108. D. A. Raichlen, A. D. Gordon, W. E. Harcourt-Smith, A. D. Foster, W. R. Haas Jr., Laetoli footprints preserve earliest evidence of human-like bipedal biomechanics. *PLOS ONE* **5**, e9769 (2010).

109. R. H. Crompton, T. C. Pataky, R. Savage, K. D’Août, M. R. Bennett, M. H. Day, K. Bates, S. Morse, W. I. Sellers, Human-like external function of the foot, and fully upright gait, confirmed in the 3.66 million year old Laetoli hominin footprints by topographic statistics, experimental footprint-formation and computer simulations. *J. Royal Soc. Interface* **9**, 707–719 (2011).

110. K. G. Hatala, N. T. Roach, K. R. Ostrofsky, R. E. Wunderlich, H. L. Dingwall, B. A. Villmoare, D. J. Green, D. R. Braun, J. W. K. Harris, A. K. Behrensmeyer, B. G. Richmond, Hominin track

assemblages from Okote Member deposits near Ileret, Kenya, and their implications for understanding fossil hominin paleobiology at 1.5 Ma. *J. Hum. Evol.* **112**, 93–104 (2017).

111. M. R. Bennett, J. W. K. Harris, B. G. Richmond, D. R. Braun, E. Mbua, P. Kiura, D. Olago, M. Kibunjia, C. Omuombo, A. K. Behrensmeyer, D. Huddart, S. Gonzalez, Early hominin foot morphology based on 1.5-million-year-old footprints from Ileret, Kenya. *Science* **323**, 1197–1201 (2009).

112. N. T. Roach, A. Du, K. Hatala, K. R. Ostrofsky, J. S. Reeves, D. R. Braun, J. W. K. Harris, A. K. Behrensmeyer, B. G. Richmond, Pleistocene animal communities of a 1.5 million-year-old lake margin grassland and their relationship to *Homo erectus* paleoecology. *J. Hum. Evol.* **122**, 70–83 (2018).

113. F. Altamura, M. R. Bennett, K. D'Août, S. Gaudzinski-Windheuser, R. T. Melis, S. C. Reynolds, M. Mussi, Archaeology and ichnology at Gombore II-2, Melka Kunture, Ethiopia: Everyday life of a mixed-age hominin group 700,000 years ago. *Sci. Rep.* **8**, 2815 (2018).

114. S. Webb, M. L. Cupper, R. Robins, Pleistocene human footprints from the Willandra Lakes, southeastern Australia. *J. Hum. Evol.* **50**, 405–413 (2006).

115. D. Bustos, J. Jakeway, T. M. Urban, V. T. Holliday, B. Fenerty, D. A. Raichlen, M. Budka, S. C. Reynolds, B. D. Allen, D. W. Love, V. L. Santucci, D. Odess, P. Willey, H. G. McDonald, M. R. Bennett, Footprints preserve terminal Pleistocene hunt? Human-sloth interactions in North America. *Sci. Adv.* **4**, eaar7621 (2018).

116. N. Panin, E. Avram, Noi urme de vertebrate in Miocenul Subcarpatilor Rominesti (Nouvelles empreintes de vertèbres dans le Miocène de la zone subcarpathique roumaine). *Studii si Cercetari de Geologie* **7**, 455–484 (1962).

117. C. Neto de Carvalho, S. Figueiredo, J. Belo, Vertebrate tracks and trackways from the Pleistocene eolianites of SW Portugal. *Comunicações Geológicas* **103**, 101–116 (2016).

118. P. McNeil, L. V. Hills, M. S. Tolman, B. Kooyman, Significance of latest Pleistocene tracks, trackways, and trample grounds from souther Alberta, Canada, in *Cenozoic Vertebrate Tracks*, S. G. Lucas, J. A. Spielmann, M. G. Lockely, Eds. (New Mexico Museum of Natural History, 2007), pp. 209–224.

119. C. Neto de Carvalho, Vertebrate tracksites from the mid-late Pleistocene eolianites of Portugal: The first record of elephant tracks in Europe. *Geol. Q.* **53**, 407–414 (2009).

120. M. P. Pasenko, Quantitative and qualitative data of footprints produced by Asian (*Elephas maximus*) and African (*Loxodonta africana*) elephants and with a discussion of significance towards fossilized proboscidean footprints. *Quat. Int.* **433**, 221–227 (2017).

121. D. Western, C. Moss, N. Georgiadis, Age estimation and population age structure of elephants from footprint dimensions. *J. Wildl. Manag.* **47**, 1192–1197 (1983).

122. W. J. Sanders, E. Gheerbrant, J. M. Harris, H. Saegusa, C. Delmer, Proboscidea, in *Cenozoic Mammals of Africa*, L. Werdelin, W. J. Sanders. Eds. (Univerity of California Press, 2010), pp. 161–252.

123. Y. Coppens, V. J. Maglio, C. T. Madden, M. Beden, Proboscidea, in *Evolution of African Mammals*, V. J. Maglio, H. B. S. Cooke, Eds. (Harvard University Press, 1978), pp. 336–367.

124. A. J. Stuart, The extinction of woolly mammoth (*Mammuthus primigenius*) and straight-tusked elephant (*Palaeoloxodon antiquus*) in Europe. *Quat. Int.* **126–128**, 171–177 (2005).

125. D. Pushkina, The Pleistocene easternmost distribution in Eurasia of the species associated with the Eemian *Palaeoloxodon antiquus* assemblage. *Mammal Rev.* **37**, 224–245 (2007).

126. N. Porat, Luminensence and electron spin resonance dating, in *Holon, a Lower Paleolithic Site in Israel*, M. Chazan, L. Kolska-Horwitz, Eds. (Peabody Museum of Archaeology and Ethnology, Harvard Univ., 2007), pp. 27–42.

127. O. Bar-Yosef, M. Belmaker, Early and middle Pleistocene faunal and hominin dispersals through southwestern Asia. *Quat. Sci. Rev.* **30**, 1318–1337 (2011).

128. J. T. Pokines, A. M. Lister, C. J. H. Ames, A. Nowell, C. E. Cordova, Faunal remains from recent excavations at Shishan Marsh 1 (SM1), a late Lower Palaeolithic open-air site in the Azraq Basin, Jordan. *Quat. Res.* **91**, 768–791 (2019).

129. A. M. Lister, W. Dirks, A. Assaf, M. Chazan, P. Goldberg, Y. H. Applbaum, N. Greenbaun, L. K. Horwitz, New fossil remains of *Elephas* from the southern levant: Implications for the evolutionary history of the Asian elephant. *Palaeogeogr. Palaeoclimatol. Palaeoecol.* **386**, 119–130 (2013).

130. A. Delagnes, C. Tribolo, P. Bertran, M. Brenet, R. Crassard, J. Jaubert, L. Khalidi, N. Mercier, S. Nomade, S. Peigné, L. Sitzia, J. F. Tournepiche, M. Al-Halibi, A. Al-Mosabi, R. MacChiarelli, Inland human settlement in southern Arabia 55,000 years ago. New Evidence from the Wadi Surdud Middle Palaeolithic site complex, western Yemen. *J. Hum. Evol.* **63**, 452–474 (2012).

131. C. Stuart, *Field Guide to Tracks and Signs of Souther, Central, and East African Wildlife* (Penguin Random House, 2013).

132. L. Liebenberg, *Photographic Guide to Tracks and Tracking in Southern Africa* (Penguin Random House, 2014).

133. H. Thomas, D. Geraads, D. Janjou, D. Vaslet, A. Memesh, D. Billiou, H. Bocherens, G. Dobigny, V. Eisenmann, M. Gayet, F. Lapparent de Broin, G. Petter, M. Halawani, First Pleistocene faunas from the Arabian peninsula: An Nafud desert, Saudi Arabia. *C. R. Acad. Sci.* **326**, 145–152 (1998).

134. M. Guagnin, C. Shipton, S. el-Dossary, M. al-Rashid, F. Moussa, M. Stewart, F. Ott, A. Alsharekh, M. D. Petraglia, Rock art provides new evidence on the biogeography of kudu (*Tragelaphus imberbis*), wild dromedary, aurochs (*Bos primigenius*) and African wild ass (*Equus africanus*) in the early and middle Holocene of north-western Africa. *J. Biogeogr.* **45**, 727–740 (2018).

135. S. G. Lucas, A. P. Hunt, Ichnotaxonomy of camel footprints, in *Cenozoic Vertebrate Tracks*, S. G. Lucas, J. A. Spielmann, M. G. Lockely, Eds. (New Mexico Museum of Natural History, 2007), pp. 155–168.

136. D. J. Meldrum, M. G. Lockley, P. G. Lukas, C. Musiba, Ichnotaxonomy of the Laetoli trackways: The earliest hominin footprints. *J. Afr. Earth Sci.* **60**, 1–12 (2011).

137. J. Y. Kim, K. S. Kim, M. G. Lockley, N. Matthews, Hominid ichnotaxonomy: An exploration of a neglected discipline. *Ichnos* **15**, 126–139 (2008).

138. R. Crassard, M. D. Petraglia, N. A. Drake, P. Breeze, B. Gratuze, A. Alsharekh, M. Arbach, H. S. Groucutt, L. Khalidi, N. Michelsen, C. J. Robin, J. Schiettecatte, Middle Palaeolithic and Neolithic occupations around Mundafan Palaeolake, Saudi Arabia: Implications for climate change and human dispersals. *PLOS ONE* **8**, e9665 (2013).

139. D. A. E. Garrod, D. M. A. Bate, *The Stone Age of Mount Carmel* (Clarendon Press, 1937).

140. O. Bar-Yosef, J. Callander, The woman from Tabun: Garrod's doubts in historical perspective. *J. Hum. Evol.* **37**, 879–885 (1999).

141. R. Grün, C. Stringer, Tabun revisited: Revised ESR chronology and new ESR and U-series analyses of dental material from Tabun C1. *J. Hum. Evol.* **36**, 601–612 (2000).

142. N. Mercier, H. Vallasas, Reassessment of the TL age estimates of burnt flints from the Paleolithic site of Tabun Cave, Israel. *J. Hum. Evol.* **45**, 401–409 (2003).

143. K. Harvati, E. N. Lopez, A 3-D look at the Tabun C2 jaw, in *Human Paleontology and Prehistory*, A. Marom, E. Hovers, Eds. (Springer, 2017), pp. 203–213.

144. Y. Shu, Q. Mei, J. Fernandez, Z. Li, N. Feng, Y. Gu, Foot morphological difference between habitually shod and unshod runnerts. *PLOS ONE* **10**, e0131385 (2015).

145. S. A. Morse, M. R. Bennett, C. Liutkus, F. Thackeray, J. McClymont, R. Savage, R. H. Crompton, Holocene footprints in Namibia: The influence of substrate on footprint morphology. *Am. J. Phys. Anthropol.* **151**, 265–279 (2013).

146. S. Webb, Further research of the Willandra Lakes fossil footprint site, southeastern Australia. *J. Hum. Evol.* **52**, 711–715 (2007).

147. M. Avanzini, P. Mietto, A. Panarello, M. D. Angelis, G. Rolandi, The Devil's Trails: Middle Pleistocene human footprints preserved in a volcanoclastic deposit of southern Italy. *Ichnos* **15**, 179–189 (2008).

148. M. Will, A. Pablos, J. T. Stock, Long-term patterns of body mass and stature evolution within the hominin lineage. *R. Soc. Open Sci.* **4**, 171339 (2017).

149. M. R. Feldesman, J. G. Kleckner, J. K. Lundy, Femur/stature ratio and estimates of stature in mid- and late-Pleistocene fossil hominids. *Yearb. Phys. Anthropol.* **83**, 359–372 (1990).

150. J.-M. Carretero, L. Rodríguez, R. García-Conzález, J.-L. Arsuaga, A. Gómez-Olivencia, C. Lorenzo, A. Bonmatí, A. Gracia, I. Martínez, R. Quam, Stature estimation from complete long bones in the middle Pleistocene humans from the Sima de los Huesos, Sierra de Atapuerca (Spain). *J. Hum. Evol.* **62**, 242–255 (2012).

151. C. B. Ruff, M. L. Burgess, N. Squyres, J.-A. Junno, E. Trinkaus, Lower limb articular scaling and body mass estimations in Pliocene and Pleistocene hominins. *J. Hum. Evol.* **115**, 85–111 (2018).

152. A. Rohatgi, Web Plot Digitizer, Verson 4.1 (2018); http://arohatgi.info/WebPlotDigitizer.

153. R. P. Jennings, J. Singarayer, E. J. Stone, U. Krebs-Kanzow, V. Khon, K. H. Nisancioglu, M. Pfeiffer, X. Zhang, A. Parker, A. Parton, H. S. Groucutt, T. S. White, N. A. Drake, M. D. Petraglia, The greening of Arabia: Multiple opportunities for human occupation of the Arabian Peninsula during the late Pleistocene inferred from an ensemble of climate model simulations. *Quat. Int.* **382**, 181–191 (2015).

154. D. Fleitmann, S. J. Burns, U. Neff, A. Mangini, A. Matter, Changing moisture sources over the last 330,000 years in northern Oman from fluid-inclusion evidence in speleothems. *Quat. Res.* **60**, 223–232 (2003).

155. D. Fleitmann, S. J. Burns, M. Pekala, A. Mangini, A. Al-Subbary, M. Al-Aowah, J. Kramer, A. Matter, Holocene and Pleistocene pluvial periods in Yemen, southern Arabia. *Quat. Sci. Rev.* **30**, 783–787 (2011).

156. J. A. Lee-Thorp, J. C. Sealy, N. J. van der Merwe, Stable carbon isotope ratio differences between collagen and bone apatite, and their relationship to diet. *J. Archaeol. Sci.* **16**, 585–599 (1989).

157. J. A. Lee-Thorp, N. J. van der Merwe, C. K. Brain, Isotopic evidence for dietary differences between two extinct baboon species from Swartkrans (South Africa). *J. Hum. Evol.* **18**, 183–190 (1989).

158. N. E. Levin, S. W. Simpson, J. Quade, T. E. Cerling, S. R. Frost, Herbivore enamel carbon isotopic composition and the environmental context of *Ardipithecus* at Gona, Ethiopia, in *The Geology of Early Humans in the Horn of Africa*, J. Quade, J. G. Wynn, Eds. (Geological Society of America Special Paper, 2008), pp. 2015–234.

159. M. Calvin, A. A. Benson, The path of carbon in photosynthesis. *Science* **107**, 476–480 (1948).

160. M. D. Hatch, C. R. Slack, H. S. Johnson, Further studies on a new pathway of photosynthetic carbon dioxide fixation in sugarcane and its occurrence in other plant species. *Biochem. J.* **102**, 417–422 (1967).

161. L. Tieszen, Natural variations in the carbon isotope values of plants: Implications for archaeology, ecology, and paleoecology. *J. Archaeol. Sci.* **18**, 227–248 (1991).

162. W. Dansgaard, Stable isotopes in precipitation. *Tellus* **16**, 436–468 (1964).

163. N. Buchmann, J. R. Ehleringer, CO_2 concentration profiles, and carbon and oxygen isotopes in C_3 and C_4 crop canopies. *Agric. For. Meteorol.* **89**, 45–58 (1998).

164. M. Sponheimer, J. A. Lee-Thorp, The oxygen isotope composition of mammalian enamel carbonate from Morea Estate, South Africa. *Oecologia* **126**, 153–157 (2001).

165. M. J. Kohn, M. J. Schoeninger, J. W. Valley, Herbivore tooth oxygen isotope compositions: Effects of diet and physiology. *Geochim. Cosmochim. Acta* **60**, 3889–3896 (1996).

166. N. E. Levin, T. E. Cerling, B. H. Passey, J. M. Harris, J. R. A. Ehleringer, Stable isotope aridity index for terrestrial environments. *Proc. Natl. Acad. Sci. U.S.A.* **103**, 11201–11205 (2006).

167. S. A. Blumenthal, L. E. Levin, F. H. Brown, J. -P. Brugal, K. L. Chritz, J. M. Harris, G. E. Jehle, T. E. Cerling, Aridity and hominin environments. *Proc. Natl. Acad. Sci. U.S.A.* **114**, 7331–7336 (2017).

168. L. B. Flanagan, J. P. Comstock, J. R. Ehleringer, Comparison of modelled and observed environmental influences on the stable oxygen and hydrogen isotope composition of leaf water in *Phaseolus vulgaris L. Plant Physiol.* **96**, 588–596 (1991).

169. M. M. Barbour, Stable oxygen isotope composition of plant tissue: A review. *Funct. Plant Biol.* **34**, 83–94 (2007).

170. Y. Wang, T. E. Cerling, A model of fossil tooth and bone diagensis: Implications for paleodiet reconstruction from stable isotopes. *Palaeogeogr. Palaeoclimatol. Palaeoecol.* **107**, 271–289 (1994).

171. J. A. Lee-Thorp, Preservation of biogenic carbon isotopic signals in Plio-Pleistocene bone and tooth mineral, in *Biogeochemical Approaches to Paleodietary Analysis*, S. H. Ambrose, M. A. Katzenberg, Eds. (Kluwer Academic/Plenum Publishers, 2000), pp. 89–115.

172. S. H. Ambrose, L. Norr, Experimental evidence for the relationship of the carbon isotope ratios of whole diet and dietary protein to those of bone collagen and carbonate, in *Prehistoric Human Bone: Archaeology at the Molecular Leval*, J. B. Lambert, G. Grupe, Eds. (Springer, 1993), pp. 1–37.

173. M. Balasse, Reconstructing dietary and environmental history from enamel isotopic analysis. Time resolution of intra-tooth sequential sampling. *Int. J. Osteoarchaeol.* **12**, 115–165 (2002)

174. M. O’Leary, Carbon isotope fractionation in plants. *Phytochemistry* **20**, 553–567 (1981).

175. K. R. Ludwig, A geochronological toolkit for Microsoft Excel (Special Publication, No. 5, Berkely Geochronological Centre, 2012).